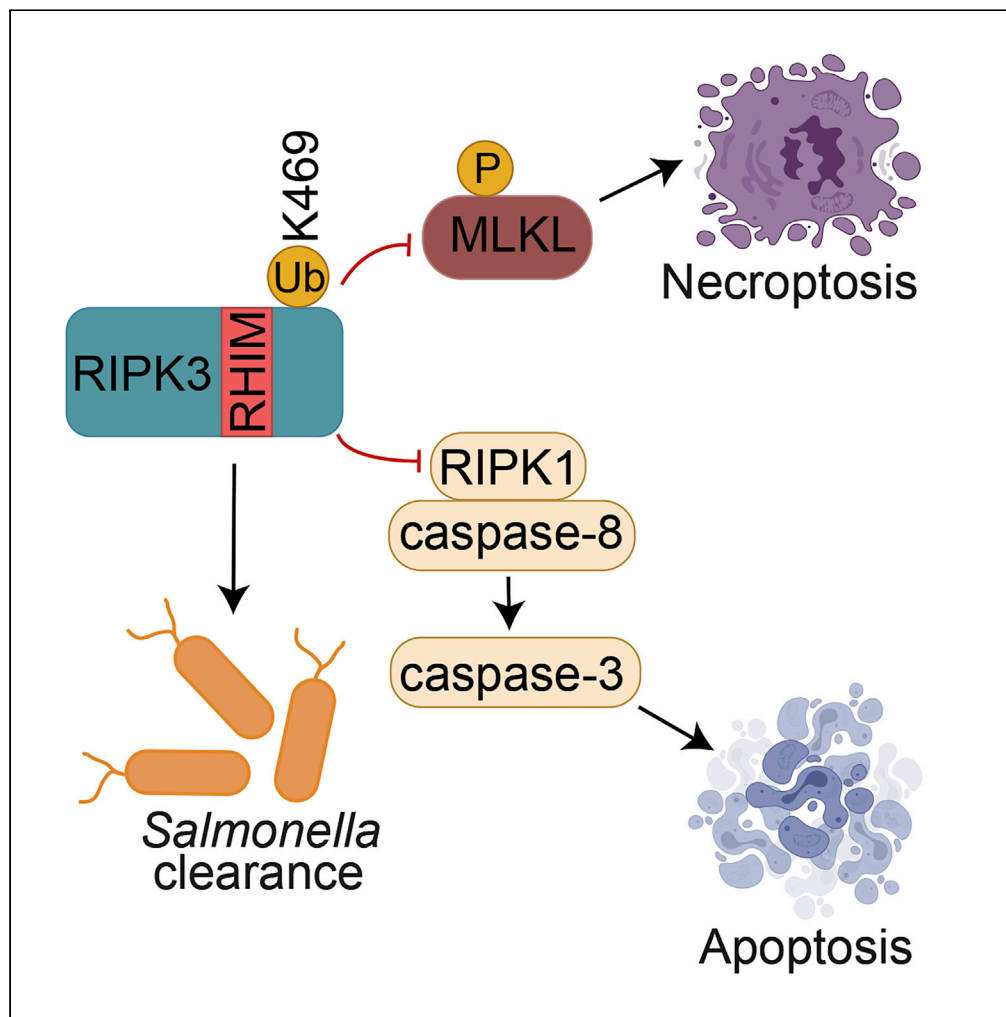# iScience

Article

Ubiquitylation of RIPK3 beyond-the-RHIM can limit RIPK3 activity and cell death

Daniel Frank,
Sarah E. Garnish,
Jarrod J. Sandow,
..., Gregor Ebert,
Jaclyn S. Pearson,
James E. Vince

vince@wehi.edu.au

Highlights

RIPK3 can be ubiquitylated on K469 to limit RIPK3-induced necroptosis and apoptosis

Ripk3[K469R/K469R] mice are more susceptible to *Salmonella* infection

Several ubiquitylated or surface exposed lysines can limit RIPK3-induced cell death

Hyper-ubiquitylated RIPK3 correlates with RIPK3 signaling and cell death

Article

Ubiquitylation of RIPK3 beyond-the-RHIM can limit RIPK3 activity and cell death

Daniel Frank,[1,2] Sarah E. Garnish,[1,2] Jarrod J. Sandow,[1,2] Ashley Weir,[1,2] Lin Liu,[1,2] Elise Clayer,[1,2,3] Lizeth Meza,[1,2] Maryam Rashidi,[1,2] Simon A. Cobbold,[1,2] Simon R. Scutts,[1,2] Marcel Doerflinger,[1,2] Holly Anderton,[1,2] Kate E. Lawlor,[4,5] Najoua Lalaoui,[1,2] Andrew J. Kueh,[1,2] Vik Ven Eng,[4,5] Rebecca L. Ambrose,[4,5] Marco J. Herold,[1,2] Andre L. Samson,[1,2] Rebecca Feltham,[1,2] James M. Murphy,[1,2] Gregor Ebert,[1,2,6] Jaclyn S. Pearson,[4,5,7] and James E. Vince[1,2,8,*]

SUMMARY

Pathogen recognition and TNF receptors signal via receptor interacting serine/threonine kinase-3 (RIPK3) to cause cell death, including MLKL-mediated necroptosis and caspase-8-dependent apoptosis. However, the post-translational control of RIPK3 is not fully understood. Using mass-spectrometry, we identified that RIPK3 is ubiquitylated on K469. The expression of mutant RIPK3 K469R demonstrated that RIPK3 ubiquitylation can limit both RIPK3-mediated apoptosis and necroptosis. The enhanced cell death of overexpressed RIPK3 K469R and activated endogenous RIPK3 correlated with an overall increase in RIPK3 ubiquitylation. *Ripk3*[K469R/K469R] mice challenged with *Salmonella* displayed enhanced bacterial loads and reduced serum IFNγ. However, *Ripk3*[K469R/K469R] macrophages and dermal fibroblasts were not sensitized to RIPK3-mediated apoptotic or necroptotic signaling suggesting that, in these cells, there is functional redundancy with alternate RIPK3 ubiquitin-modified sites. Consistent with this idea, the mutation of other ubiquitylated RIPK3 residues also increased RIPK3 hyper-ubiquitylation and cell death. Therefore, the targeted ubiquitylation of RIPK3 may act as either a brake or accelerator of RIPK3-dependent killing.

INTRODUCTION

Caspase-independent programmed necrosis, termed necroptosis, has emerged as an important host response against microbial infections and a potential disease driver in conditions associated with exacerbated cell death-induced inflammation, such as kidney ischemia-reperfusion injury (Galluzzi et al., 2017; Muller et al., 2017; Newton et al., 2016a; Pefanis et al., 2019). As such, there is significant interest in understanding the molecular determinants that regulate the necroptotic machinery, and how this might be therapeutically exploited to develop new treatments for infections, cancer and cell death-associated inflammatory conditions (Murphy and Vince, 2015).

Necroptosis is elicited by both pathogen recognition receptors, such as toll-like receptors (TLRs), the DNA sensor Z-DNA-binding protein 1 (ZBP1), and death receptors, such as TNF Receptor 1 (TNFR1). In the absence of inhibitor of apoptosis (IAP) proteins and/or caspase-8, these receptors can engage receptor interacting serine/threonine protein kinase-3 (RIPK3) (Cho et al., 2009; He et al., 2009, 2011; Kaiser et al., 2013; Upton et al., 2012; Zhang et al., 2009). RIPK3 recruitment occurs through homotypic interactions via common receptor-interacting protein homotypic interaction motifs (RHIMs) (Sun et al., 2002) found in the related TNFR1 signaling adaptor RIPK1, in ZBP1, and also the TLR3 and TLR4 cytoplasmic adaptor, TIR-domain-containing adapter-inducing IFN-β (TRIF) (Silke et al., 2015). Subsequently, RHIM-mediated oligomerization of RIPK3 and its autophosphorylation (T231/S232 in mouse or S227 in human) allows it to phosphorylate and thereby activate the terminal effector of necroptotic cell death, mixed lineage kinase domain-like (MLKL) protein (Chen et al., 2013; Garnish et al., 2021; Murphy et al., 2013; Petrie et al., 2018; Sun et al., 2012). Activated MLKL associates with, and damages, the plasma membrane to cause osmotic swelling and the eventual cellular rupture that triggers the
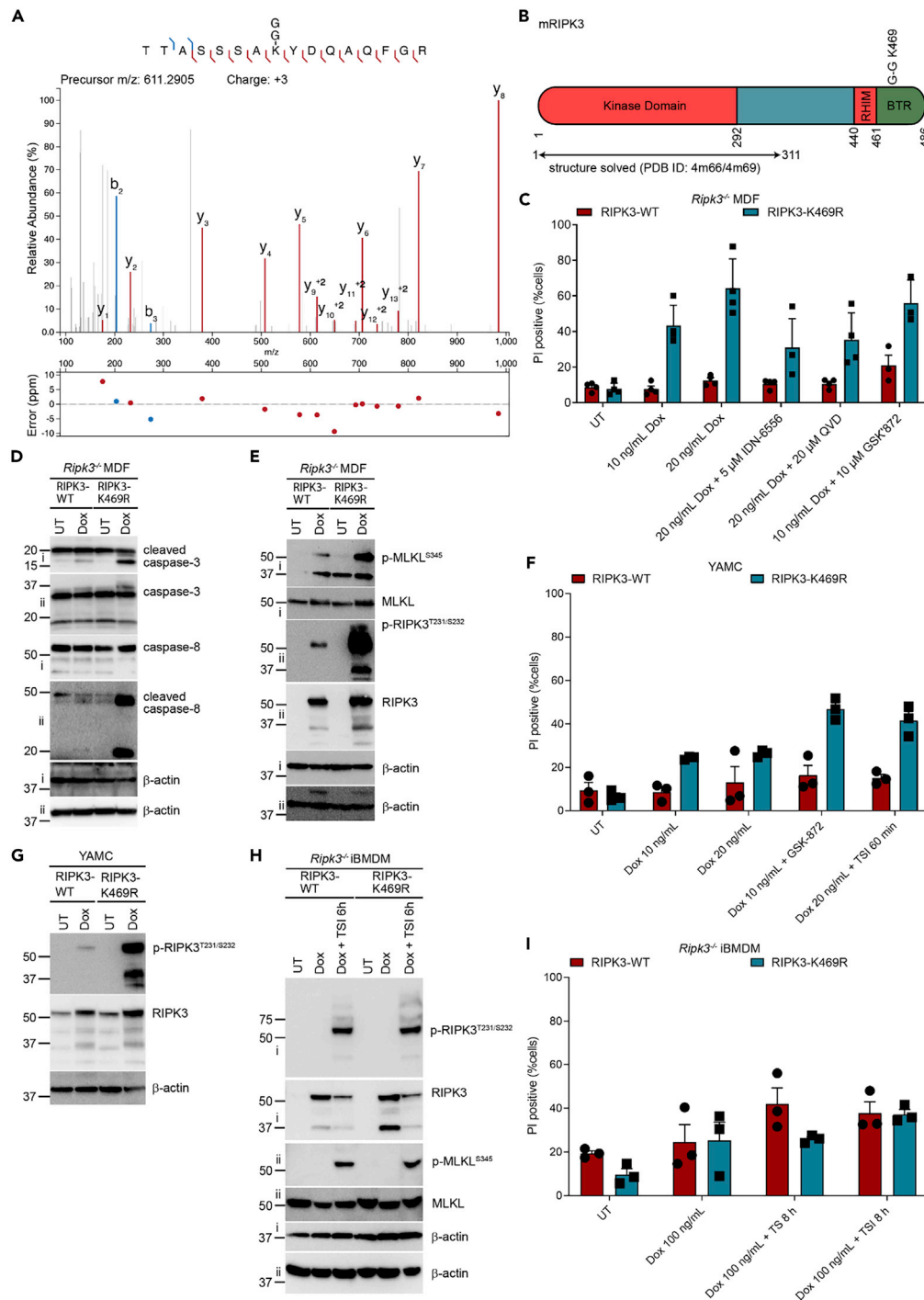
Figure 1. Mouse RIPK3 is ubiquitylated beyond-the-RHIM (BTR) on K469 to restrict apoptosis and necroptosis in a cell type-dependent manner

(A) LC-MS/MS analysis of FLAG-purified RIPK3-WT following doxycycline (dox)-induced expression in $Ripk3^{-/-}$ MDFs for 16–18 h identified a diGly motif on K469.

(B) The domain architecture of mouse RIPK3. The K469 diGly motif is situated at the C-terminal, 8 amino acids beyond-the-RHIM (BTR). No structural information is available for this region, although it is predicted to be disordered.

(C) The expression of stably integrated RIPK3-WT or RIPK3-K469R-complemented $Ripk3^{-/-}$ MDFs was induced with dox for 16–18 h in the presence of the pan-caspase inhibitors IDN-6556 or QVD-OPh, or the RIPK3 kinase inhibitor GSK'872, as

Figure 1. *Continued*

indicated. Cell death was measured by propidium iodide (PI) uptake and flow cytometry. Results are represented as mean ± SEM of 3–4 independent experiments (symbols).

(D and E) The expression of stably integrated RIPK3-WT or RIPK3-K469R in *Ripk3*$^{-/-}$ MDFs was induced by 20 ng/mL dox treatment for 16–18 h, and cells were subsequently analyzed by western blotting of total cell lysates. Roman numerals to the left of blots (i, ii, and iii) indicate the membrane probed for samples run in triplicate. Data are representative of three independent experiments.

(F–I) Stably integrated RIPK3-WT or RIPK3-K469R expression was induced with 20 ng/mL dox treatment in *Ripk3*$^{-/-}$ mouse colonic epithelium (YAMC) cells (F and G) or 100 ng/mL dox in iBMDMs (H and I) for 16–18 h, and cells were subsequently analyzed by western blotting of total cell lysates or cell death measured by propidium iodide (PI) uptake and FACS. In the case of YAMCs, cells were treated with or without 10 μM of the RIPK3 kinase inhibitor GSK'872, or in the last 1 h stimulated with TSI, as indicated. For iBMDMs, cells were also treated with TS or TSI for 6 h (western blot), or for 8 h (PI analysis). Data are represented as the mean ± SEM of 3 independent experiments (symbols; F and I), or representative of 3 independent experiments (G and H). See also Figures S1 and S2.

release of immunogenic damage-associated molecular patterns (Dondelinger et al., 2014; Hildebrand et al., 2014; Murai et al., 2018; Samson et al., 2020; Wang et al., 2014).

Although RIPK3 kinase activity is essential for necroptosis, RIPK3 can also signal activation of apoptotic caspase-8. For example, genetic deficiency or chemical targeting of the IAP proteins results in TLR- or TNFR1-induced RIPK3 signaling that promotes caspase-8-mediated apoptosis (Lawlor et al., 2015; Vince et al., 2012; Yabal et al., 2014). RIPK3-induced caspase-8 activation can also arise from exposure to RIPK3 kinase inhibitors or introduction of kinase-dead mutations to promote RIPK3 binding to RIPK1, leading to RIPK1 death domain recruitment of the adaptor FADD, which then engages caspase-8 to form a complex often referred to as the Ripoptosome (Feoktistova et al., 2011; Mandal et al., 2014; Newton et al., 2014; Tenev et al., 2011). Apart from its classical role in cell death, RIPK3 can also trigger inflammatory signaling pathways, such as the induction of NF-κB (Moriwaki et al., 2014) and activation of the NLRP3 inflammasome to drive IL-1β maturation and inflammation (Conos et al., 2017; Duong et al., 2015; Kang et al., 2013; Lawlor et al., 2015, 2017; Polykratis et al., 2019; Vince et al., 2012; Yabal et al., 2014). Numerous mouse models of disease, mostly through genetic deletion studies, have alluded to RIPK3-induced apoptotic and/or necrotic death as an important mediator of tissue damage (Orozco and Oberst, 2017; Silke et al., 2015).

RIPK3 signaling is regulated by various post-translational modifications (PTMs) (Meng et al., 2021), such as ubiquitylation (Choi et al., 2018; Lee et al., 2019; Moriwaki and Chan, 2016; Onizawa et al., 2015; Seo et al., 2016), phosphorylation (Chen et al., 2013; Sun et al., 2012), S-nitrosylation (Miao et al., 2015), and *O*-GlcNA-cylation (Giogha and Lawlor, 2019; Li et al., 2019). Studies to date have identified a number of ubiquitylation sites on RIPK3, most of which are associated with RIPK3 turnover by the proteasome (Choi et al., 2018; Moriwaki and Chan, 2016) or the lysosome (Lim et al., 2019; Seo et al., 2016) whereas others suggest a role for ubiquitylation in tuning RIPK3 complex assembly (Lee et al., 2019; Onizawa et al., 2015; Roedig et al., 2021).

Here, we identify a new RIPK3 ubiquitylation site and characterize its role in RIPK3-induced cell death. We show that mouse RIPK3 is decorated by ubiquitin on lysine 469 (K469), which is situated 8 amino acids beyond-the-RHIM (BTR) on the C-terminal end of RIPK3. The loss of RIPK3 K469 ubiquitylation promoted RIPK3 hyper-ubiquitylation mediated, in part, by ubiquitin decoration of K359, and triggered enhanced RIPK3-mediated signaling. Mutant *Ripk3*$^{K469R/K469R}$ mice were less efficient at clearing *Salmonella* infections *in vivo*, although *Ripk3*$^{K469R/K469R}$-expressing macrophages and fibroblasts displayed normal cell death responses, suggesting that alternate RIPK3 ubiquitylation sites also act to repress RIPK3-mediated cell death in a stimulus and cell type-specific manner.

RESULTS

RIPK3 is ubiquitylated beyond-the-RHIM(BTR) on lysine 469

To identify RIPK3 residues that are targeted for post-translational modification (PTM), we reconstituted immortalized *Ripk3*$^{-/-}$ mouse dermal fibroblasts (MDFs) with a stably integrated, doxycycline (dox)-inducible, FLAG-tagged wildtype (WT) RIPK3 (denoted hereafter as RIPK3-WT) construct. Following the addition of dox to induce RIPK3 expression (which was moderately overexpressed relative to endogenous RIPK3; Figure S1A), RIPK3 was immunoprecipitated using an anti-FLAG antibody. Subsequent mass spectrometry analysis of trypsin-digested RIPK3-WT identified a Lys-ε-Gly-Gly (diGly) remnant on residue 469, which is

situated 8 amino acids beyond the RHIM (BTR) of mouse RIPK3 (Figures 1A and 1B). The presence of the diGly motif on RIPK3 K469 indicates that this lysine is targeted for ubiquitylation upon expression of RIPK3 alone, in the absence of an external cell death stimulus. Alignment of RIPK3 sequences showed that K469 is conserved in mouse and rat RIPK3 but not human RIPK3 (Figure S1B).

To confirm that the diGly remnant found on RIPK3-K469 represents ubiquitylation, the ubiquitylated proteome of $Ripk3^{-/-}$ MDFs expressing RIPK3-WT was purified using a recombinant GST-Ubiquitin–associated (UBA) domain. Consistent with RIPK3 being ubiquitylated, the purified ubiquitylated proteome contained high molecular weight RIPK3 laddering (Figure S1C). Importantly, treatment with USP21, a pan-deubiquitylating enzyme, collapsed the high molecular weight laddering of RIPK3, thereby demonstrating that RIPK3 is modified predominantly with ubiquitin chains, not other ubiquitin-like modifiers (Figure S1C). Consistent with this idea, only the co-expression of HA-tagged ubiquitin with RIPK3-WT in 293T cells, but not the other HA-tagged ubiquitin-like proteins, Sumo2 and Sumo3, could co-precipitate high molecular weight, laddered, RIPK3 (Figure S1D).

RIPK3-K469 ubiquitylation limits necroptosis and apoptosis

To examine the functional impact of RIPK3-K469 ubiquitylation, we generated a mutant RIPK3 with a lysine to arginine substitution at K469, RIPK3-K469R, to abolish its ability to be ubiquitylated while retaining a positive charge at this site. $Ripk3^{-/-}$ MDFs were reconstituted with a stably integrated, dox-inducible, RIPK3-WT or RIPK3-K469R construct. Dox treatment alone to induce RIPK3 expression resulted in accelerated cell death in RIPK3-K469R-expressing cells compared to RIPK3-WT-expressing cells, as measured by propidium iodide (PI) uptake and flow cytometry (Figure 1C), and in long-term (7 days) clonogenic survival assays (Figure S1E). As expected, treatment of RIPK3-WT with the necroptotic stimuli TSI (TNF, smac-mimetic, and IDN-6556) led to a marked increase in cell death, thereby demonstrating that RIPK3-WT could function normally to signal cell death (Figure S1F). Altogether, these data suggest that RIPK3-K469 ubiquitylation limits RIPK3-induced cell death signaling.

In mice, RIPK3 auto-phosphorylation on T231 and S232 allows RIPK3 to phosphorylate MLKL on S345, which causes MLKL activation and necroptosis (Murphy et al., 2013). However, RIPK3 can also signal apoptosis independent of its kinase activity, via RHIM-mediated recruitment of RIPK1 and activation of caspase-8 (Mandal et al., 2014; Newton et al., 2014). Therefore, to define the type of cell death induced by RIPK3-K469R expression, MDFs were treated with pan-caspase inhibitors, IDN-6556 or QVD-OPh, which block apoptosis and promote necroptosis, or with the RIPK3 kinase inhibitor, GSK'872, which blocks necroptosis but not RIPK3-triggered, caspase-8-mediated apoptosis. Pan-caspase inhibition moderately reduced RIPK3-K469R-mediated killing (Figure 1C). However, compared to RIPK3-WT, enhanced cell killing was still observed on RIPK3-K469R expression in both caspase-inhibited cells and in cells treated with GSK'872 (at a dose that does not cause apoptosis in RIPK3-WT expressing cells or in RIPK3 deficient MDFs, Figures 1C and S1G). These data suggest that RIPK3-K469R can engage in both apoptosis and necroptosis signaling.

Consistent with apoptosis and necroptosis activation, the expression of RIPK3-K469R alone resulted in increased caspase-8 and -3 cleavage, and RIPK3 and MLKL phosphorylation at T231/S232 and S345, respectively, when compared to RIPK3-WT (Figures 1D and 1E). Moreover, quantitative mass spectrometry of FLAG-purified RIPK3-WT and RIPK3-K469R identified numerous RIPK3 phosphorylation sites previously implicated in RIPK3 signaling (Meng et al., 2021). These sites were enriched on RIPK3-K469R compared to RIPK3-WT, including T231/S232 (required for MLKL activation) and two novel sites, T386 and T407, of undetermined function (Figures S2A and S2B).

We next assessed the impact of abolishing RIPK3-K469 ubiquitylation on RIPK3 activity at the single-cell level by confocal microscopy. Consistent with the above findings, expression of mutant RIPK3-K469R alone drove a marked increase in cytosolic p-RIPK3$^{T231/S232}$, while overall RIPK3 expression levels between RIPK3-WT and RIPK3-K469R-expressing cells remained comparable (Figures S2C and S2D). Of note, the detection of p-RIPK3$^{T231/S232}$ in the cytosol was not present in all cells equally at any single time point. This suggests the kinetics of RIPK3 autophosphorylation varies between cells within the population, consistent with population-level cell death responses.

To investigate the role of RIPK3 K469 in alternate cell types, we expressed both RIPK3-WT and RIPK3-K469R in immortalized young adult mouse colonic epithelium (YAMC) and immortalized bone marrow-derived

macrophage (iBMDM) cell lines. Similar to immortalized MDFs, the expression of RIPK3-K469R in YAMC cells also enhanced cell death when cells were treated with necroptosis inhibitor GSK'872 or the necroptotic stimuli TSI (Figure 1F) and resulted in more RIPK3 T231/S232 phosphorylation (Figure 1G). Unlike YAMC cells, however, RIPK3-K469R did not trigger RIPK3 hyperphosphorylation when expressed in *Ripk3*$^{-/-}$ iBMDMs, and these cells were not sensitized to TS-induced apoptosis or TSI-induced necroptosis (Figures 1H and 1I). These results suggest that in cell types capable of RIPK3 autophosphorylation by overexpression alone, such as immortalized MDFs and YAMCs, mutant RIPK3-K469R increases its oligomerization and/or scaffolding activity which promotes both caspase-8 recruitment and apoptosis, in addition to RIPK3 autophosphorylation and necroptosis.

RIPK3-K469 ubiquitylation does not impact RIPK3 turnover

Several ubiquitylation sites on RIPK3 have been implicated in targeting RIPK3 for lysosomal or proteasomal degradation (Ali and Mocarski, 2018; Lim et al., 2019; Moriwaki and Chan, 2016; Seo et al., 2016). We therefore asked if the hyperactivation of RIPK3-K469R results from reduced protein turnover. *Ripk3*$^{-/-}$ MDFs reconstituted with dox-inducible WT or mutant RIPK3-K469R were treated with dox for 16–18h, and *de novo* RIPK3 transcription was subsequently prevented by removing dox from the media before analysis by western blotting. Both RIPK3-WT and RIPK3-K469R protein levels were observed to diminish at a similar rate on dox removal, suggesting that RIPK3-K469 ubiquitylation does not play a role in regulating RIPK3 turnover (Figures 2A and 2B).

Consistent with previous observations (Ali and Mocarski, 2018; Moriwaki and Chan, 2016), the inhibition of the proteasome with MG132 resulted in the accumulation of ubiquitylated RIPK3, indicating that RIPK3 is targeted for proteasomal degradation at steady state (Figures 2C and S2E). However, upon the activation of necroptosis, pre-treatment of MDFs with MG132 had little impact on RIPK3-driven cell death (Figure S2F). The inhibition of lysosome function using Bafilomycin A1, on the other hand, had no impact on steady-state, or ubiquitylated, RIPK3 levels (Figure 2C). Therefore, it is unlikely that RIPK3-K469 ubiquitylation limits RIPK3 killing activity by targeting RIPK3 for lysosomal or proteasomal degradation.

The activation of RIPK3 correlates with increased RIPK3 ubiquitylation levels

Previous studies suggest that the substitution of RIPK3 lysine sites targeted for ubiquitylation with arginine reduces overall levels of RIPK3 modified with ubiquitin chains (Choi et al., 2018; Lee et al., 2019; Moriwaki and Chan, 2016; Seo et al., 2016). We therefore asked if the loss of ubiquitylation on RIPK3-K469 also caused a reduction in RIPK3 ubiquitylation by purifying the ubiquitylated proteome using Tandem Ubiquitin Binding Entities (TUBEs) (Hjerpe et al., 2009), which allows the detection of overall RIPK3 ubiquitylation levels by western blot. Unexpectedly, when compared to RIPK3-WT, the total ubiquitylation of RIPK3-K469R, including the ubiquitylation of T231/S232-phosphorylated RIPK3-K469R, was enhanced (Figure 2D), which correlated with its increased killing capacity (Figure 1C). Blocking RIPK3 kinase activity and hence T231/S232 autophosphorylation with GSK'872 did not prevent RIPK3 ubiquitylation (Figure 2E). This demonstrates that RIPK3 ubiquitylation can occur in the absence of RIPK3 kinase activity and that it might precede RIPK3 phosphorylation. Moreover, RIPK3 ubiquitylation did not occur as a result of membrane damage and/or necroptotic cell death, as MLKL was dispensable for endogenous RIPK3 ubiquitylation upon TSI-induced necroptosis signaling (Figure 2F). The ubiquitylation of RIPK3-K469R was also not impacted by the loss of RIPK1 kinase activity, as demonstrated by the treatment of cells with the RIPK1 kinase-specific inhibitor, Nec-1s, before dox-induced RIPK3-K469R expression and TUBE purification (Figure 2G).

Activated and ubiquitylated RIPK3 transitions into a detergent insoluble cellular fraction

Activated MLKL associates with the plasma membrane, and potentially other intracellular membranes, to induce cell death (Dondelinger et al., 2014; Hildebrand et al., 2014; Samson et al., 2020, 2021; Wang et al., 2014). To study if cytosolic RIPK3 might also change in cellular localization upon ubiquitylation and activation, we examined RIPK3 partitioning into Triton-X-100 (TX-100) detergent-soluble and-insoluble fractions. Following dox-induced expression in *Ripk3*$^{-/-}$ MDFs or YAMCs, the majority of RIPK3-WT, RIPK3-K469R and MLKL was detected in the TX-100-soluble fraction (Figures 3A and S3A). However, active and ubiquitylated RIPK3, and phosphorylated MLKL, partitioned preferentially into a TX-100-insoluble fraction, and this transition was elevated in RIPK3-K469R-expressing cells (Figures 3A and S3A). In WT MDFs, necroptosis activation by TSI treatment also resulted in the migration of endogenous ubiquitylated p-RIPK3$^{T231/S232}$
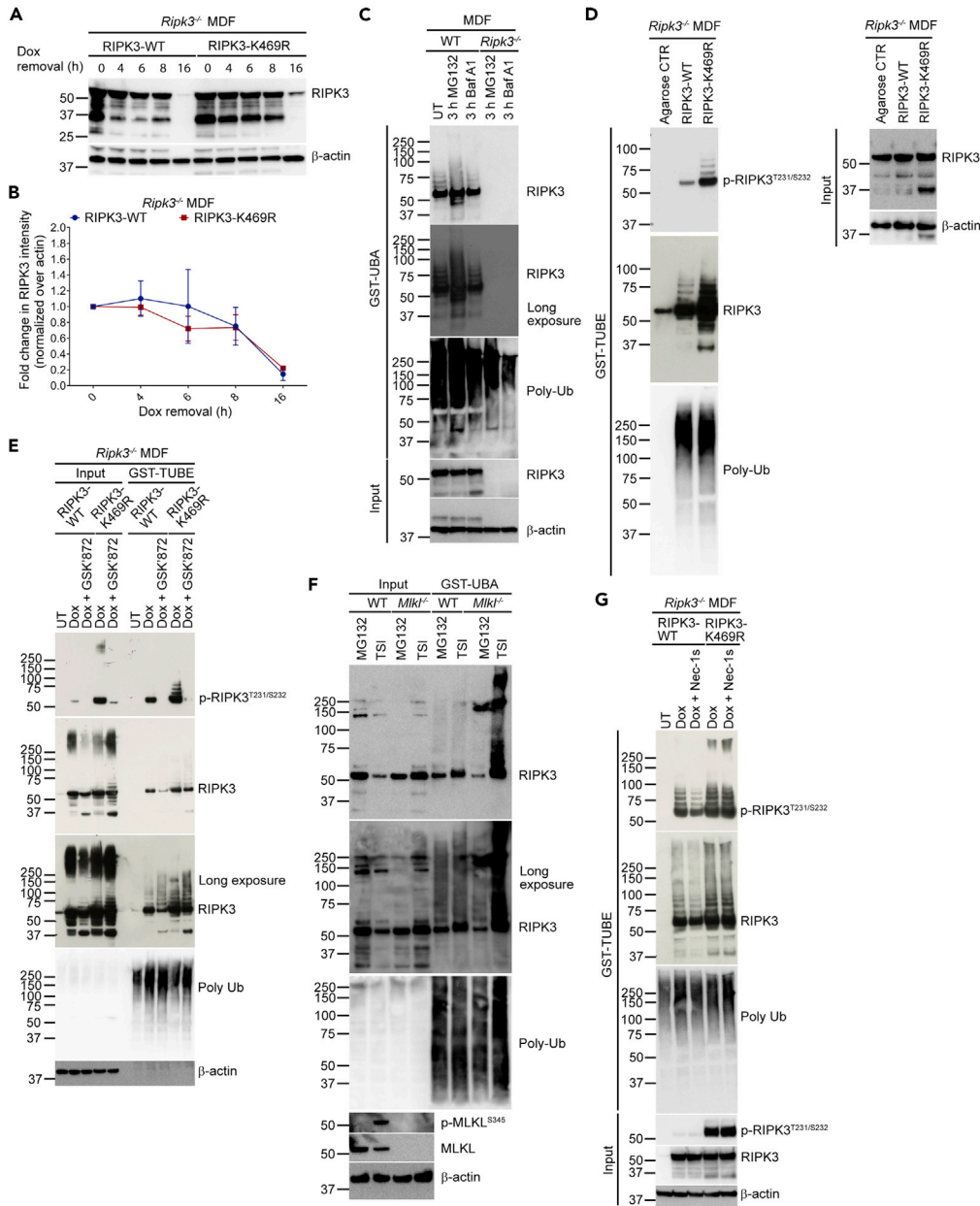
Figure 2. Ubiquitylation of RIPK3-K469 prevents overall increases in RIPK3 ubiquitylation

(A) $Ripk3^{-/-}$ MDFs containing RIPK3-WT or RIPK3-K469R were treated with 5 ng/mL dox for 16–18 h. Cells were washed to remove dox and subsequently RIPK3 levels were analyzed at the indicated time points by western blotting. Data are representative of 4 independent experiments.

(B) Densitometry analysis of (A). Levels of RIPK3 were quantified by Image Lab software (Biorad). Results are represented as mean ± SEM of 3 independent experiments.

(C and F) Where indicated, WT, $Mlkl^{-/-}$, and $Ripk3^{-/-}$ MDFs were treated with 20 μM MG-132, 100 nM Baf-A1, or the necroptotic stimuli TSI (100 ng/mL TNF, 1 μM Cp.A, and 5 μM IDN-6556) for 3 h, harvested for GST-UBA pull-down, and subsequently analyzed by western blotting.

(D, E, and G) $Ripk3^{-/-}$ MDFs containing stably integrated dox-inducible RIPK3-WT or RIPK3-K469R were treated with 20 ng/mL dox for 16–18 h (D) with or without 10 μM of the RIPK3 kinase inhibitor GSK'872 (E) or 10 μM of the RIPK1 kinase inhibitor Nec-1s (G). A GST-TUBE pull-down was subsequently performed and samples analyzed by western blotting. All results (C-G) are representative of 3 independent experiments. See also Figure S2.
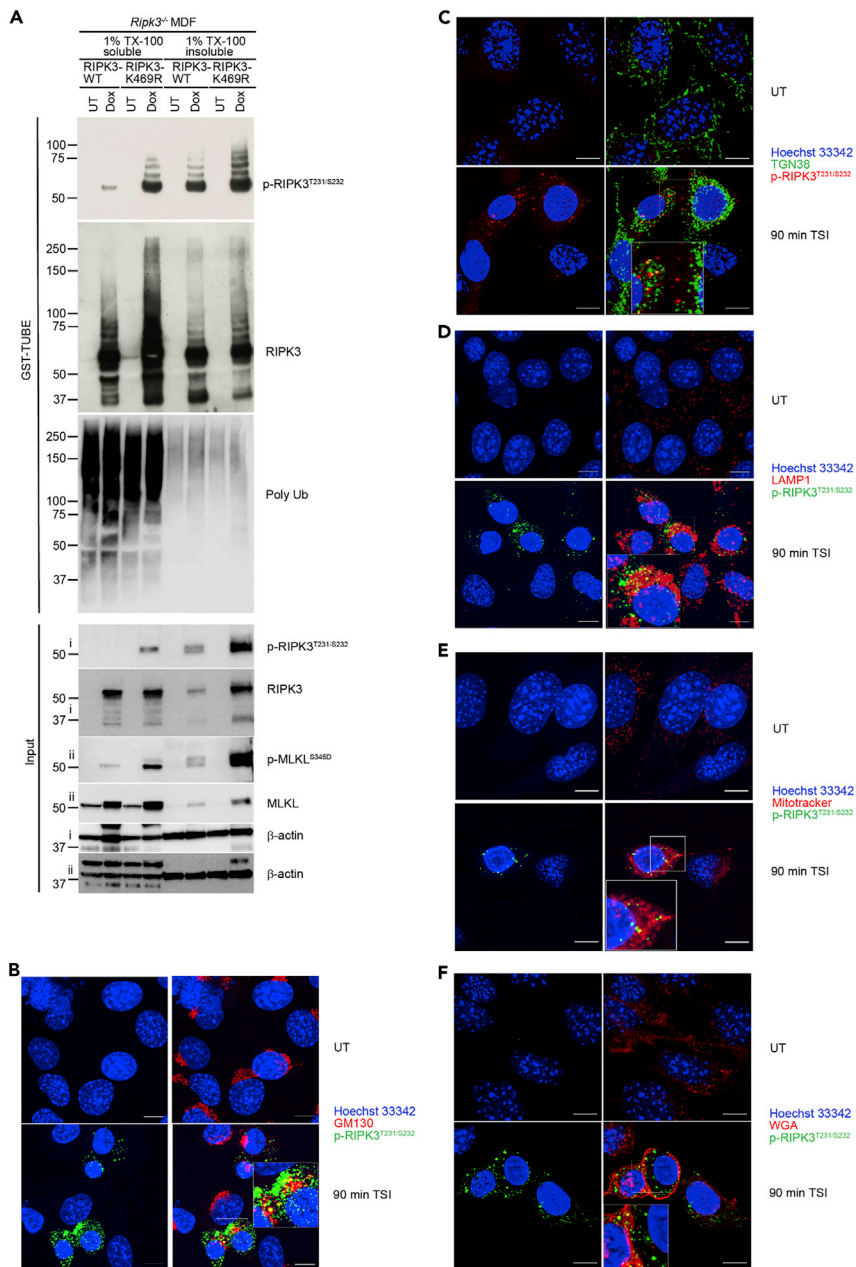
Figure 3. Activated RIPK3 transitions into a TX-100-insoluble compartment

(A) $Ripk3^{-/-}$ MDFs containing stably integrated dox-inducible RIPK3-WT or RIPK3-K469R were treated with 20 ng/mL dox for 16–18 h. Lysates were subsequently separated into 1% TX-100-soluble or -insoluble fractions before GST-TUBE pull-down and analysis by western blotting. Roman numerals to the left of blots (i, ii) indicate the membrane probed. Data are representative of 4 independent experiments. See also Figure S3A for YAMC cell line analysis.

(B–F) MDFs were stimulated with the necroptotic stimuli 100 ng/mL TNF (T),1 μM Cp.A (S), and 5 μM IDN (I) (TSI) for 90 min before immunofluorescence analysis with p-RIPK3$^{T231/S232}$ and the indicated organelle markers. Scale bars are 10 μm. Data are representative of 3 independent experiments. WGA; wheat germ agglutinin. See also Figure S3.

into the TX-100 insoluble fraction within 90 min (Figure S3B), akin to hyperactivated RIPK3-K469R (Figure 3A).

We next assessed whether activated RIPK3 is associated with a particular organelle during necroptosis by examining the localization of endogenous p-RIPK3$^{T231/S232}$ levels by confocal microscopy in WT MDFs after

TSI treatment. Notably, we did not find any substantial colocalization of TSI-induced endogenous p-RIPK3$^{T231/S232}$ with the nucleus (Hoechst 33342), Golgi (GM130 and TGN38), lysosome (LAMP1), mitochondria (Mitotracker), or plasma membrane/endosomes (WGA) (Figures 3B–3F). These results suggest that the loss of RIPK3-K469 ubiquitylation, or TSI-induced endogenous RIPK3 triggering, results in the re-distribution of activated and ubiquitylated RIPK3 into a TX-100-insoluble compartment that may resemble a membraneless organelle (Chen et al., 2013; He et al., 2009; Samson et al., 2021).

Macrophages and dermal fibroblasts derived from *Ripk3*$^{K469R/K469R}$ mice display no alterations in RIPK3-driven cell death

To study the impact of losing RIPK3-K469 ubiquitylation *in vivo* we generated *Ripk3*$^{K469R/K469R}$ mice by CRISPR/Cas9 technology on a C57BL/6J background. The generation of founder RIPK3 mutant mice was confirmed by next-generation sequencing and these founders were subsequently backcrossed onto WT C57BL/6J mice for two generations before experimentation.

Ripk3$^{K469R/K469R}$ animals displayed no overt phenotype compared to *Ripk3*$^{+/+}$ control mice, and western blot analysis of various tissues showed no difference between endogenous RIPK3 and RIPK3^{K469R} expression (Figures S3C–S3H). Advia hematology analysis revealed no substantial differences in white and red blood cell compartments in *Ripk3*$^{K469R/K469R}$ mice, compared to *Ripk3*$^{+/+}$ and *Ripk3*$^{+/K469R}$ controls (data not shown). Therefore, abolishing K469 ubiquitylation on RIPK3 does not perturb basal cellular physiology, although mice were not examined for an age-related phenotype, which has been observed in some animals with over-active RIPK3 (Lee et al., 2019).

In vitro experiments complementing RIPK3-deficient cells with the overexpression of RIPK3-K469R suggested that ubiquitylation on K469 is important to restrict RIPK3-induced cell death in immortalized fibroblast and colonic cell lines, but not in phagocytic cells such as macrophages (Figures 1C–1I and S1E). We therefore treated BMDMs and primary MDFs with TS, which triggers RIPK3-mediated apoptosis (Figure S4A) (Lawlor et al., 2015) or with TSI to induce RIPK3-MLKL signaling and necroptosis. However, both *Ripk3*$^{+/+}$ and *Ripk3*$^{K469R/K469R}$ macrophages and fibroblasts died comparably following the activation of RIPK3-driven apoptosis or necroptosis, even when IFNβ priming was used to increase the necroptotic response (Figures S4B and S4C). Therefore, alternate RIPK3 ubiquitylation sites may act in place of, or in a co-operative manner with, RIPK3 K469 ubiquitylation to limit its capacity to cause cell death.

Ripk3$^{K469R/K469R}$ mice display a moderately reduced capacity to clear *Salmonella* infection

We hypothesized that despite normal *Ripk3*$^{K469R/K469R}$ fibroblast and macrophage death responses, RIPK3-K469 ubiquitylation may still have a stimulus or cell-specific role *in vivo*. Cell death, and RIPK3, have previously been implicated in *Salmonella* infection (Doerflinger et al., 2020; Dong et al., 2022; Robinson et al., 2012; Satkovich et al., 2020; Shutinoski et al., 2020). We first assessed if BMDMs derived from *Ripk3*$^{K469R/K469R}$ animals were more susceptible to cell death resulting from *Salmonella* sensing *in vitro*. However, macrophages derived from *Ripk3*$^{+/+}$ and *Ripk3*$^{K469R/K469R}$ mice died at comparable rates upon *Salmonella* infection, even in the presence of a pan-caspase inhibitor to promote necroptotic signaling (Figures S4D and S4E). Therefore, to ascertain if altered ubiquitylation of RIPK3-K469 impacted the immune response to *Salmonella*, we challenged *Ripk3*$^{+/+}$ and *Ripk3*$^{K469R/K469R}$ mice with a low intravenous (iv) dose (100 CFU) of the growth-attenuated strain of *Salmonella*; *Salmonella enterica* serovar Typhimurium strain BRD509 (denoted hereafter as *Salmonella*) (Strugnell et al., 1992), and measured bacterial burdens and systemic inflammatory cytokine production. This *Salmonella* strain models the initial infection and recovery phases of disease. In both phases, the innate immune system and T-cells are critical to limit pathogen burden and promote bacterial clearance (Benoun et al., 2018; Kupz et al., 2014). Of note, this dose of *Salmonella* does not overcome stomach acidity and therefore bacterial colonization of the small intestine is not observed.

Interestingly, *Ripk3*$^{K469R/K469R}$ mice displayed moderately increased bacterial numbers in the spleen and liver 2 weeks post-infection when compared to WT control animals (Figures 4A and 4B), although organ weights were comparable across genotypes (Figures 4C and 4D). Measurement of serum cytokine and chemokine levels in *Salmonella*-infected *Ripk3*$^{K469R/K469R}$ mice revealed reduced IFNγ and elevated MCP-1 (CCL2) relative to *Ripk3*$^{+/+}$ animals (Figures 4E and 4F) whereas other cytokines, TNF, IL-6, IL-12, and IL-10 were comparable between genotypes (Figures 4G–4J). Because IFNγ is important for the control of *Salmonella* infection (Kupz et al., 2014), its reduced levels in *Ripk3*$^{K469R/K469R}$ mice may explain their elevated bacterial burdens. In addition, Advia hematology analysis post-infection revealed elevated white blood cell (WBC) counts in *Ripk3*$^{K469R/K469R}$ animals, reflecting increased lymphocytes whereas levels of monocytes,
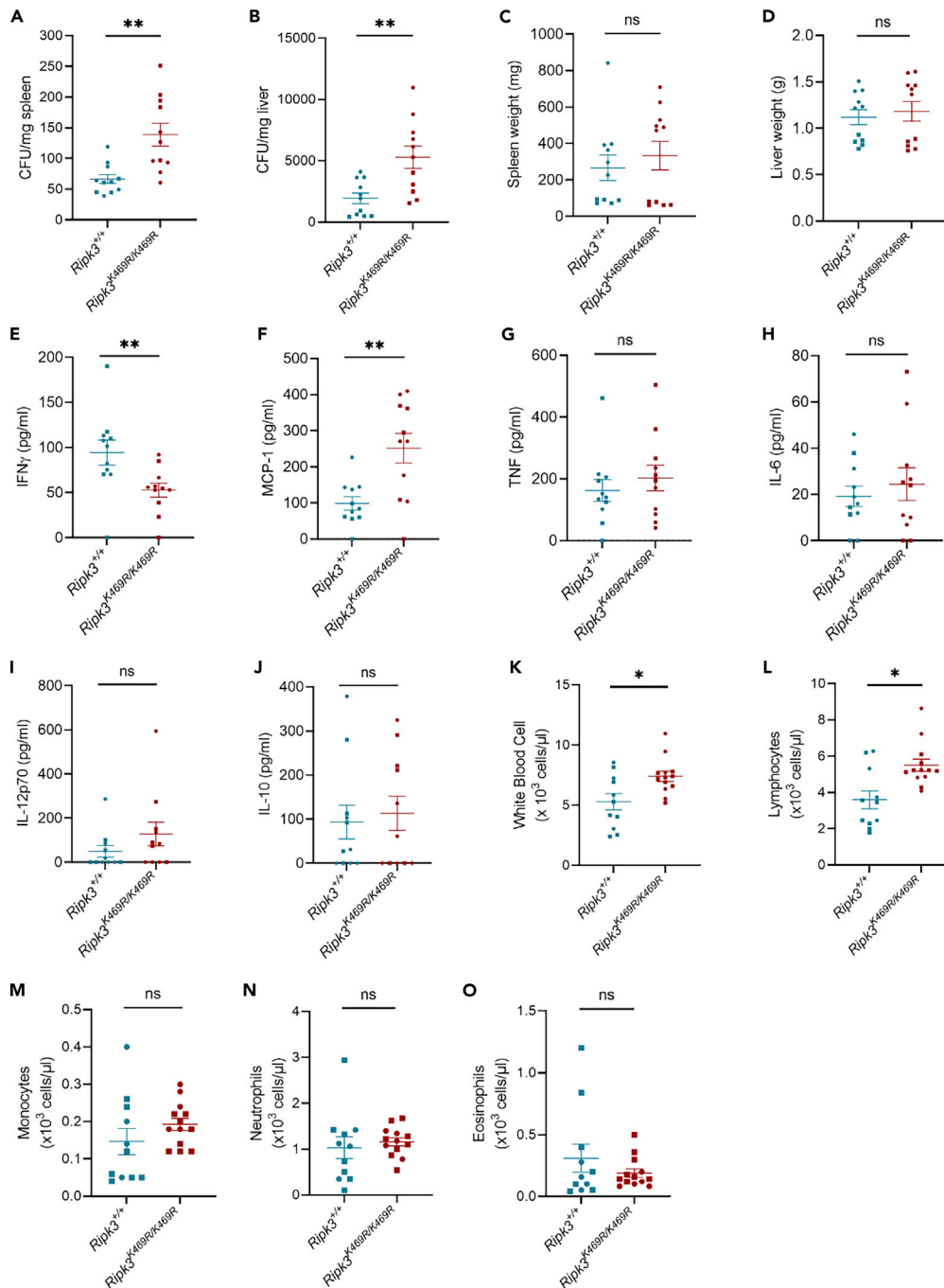
Figure 4. RIPK3-K469 ubiquitylation promotes *Salmonella* clearance

(A) *Ripk3⁺/⁺* and *Ripk3^K469R/K469R* mice were intravenously infected with *Salmonella* (100 CFU) and assessed for bacterial loads in the spleen (A) and liver (B) and their respective organ weights (C and D) at day 14 post-infection.

(E–O) Concentration of cytokines in mouse sera at day 14 after infection as measured by CBA (E–J), or Advia hematology analysis of cell numbers (K–O). All results are depicted as mean ± SEM of 11–12 mice per genotype, pooled from 2 independent experiments (reflected by different symbols). *p < 0.05; **p < 0.01; ns: not significant (Mann-Whitney test). CFU; colony forming units. See also Figures S3 and S4.
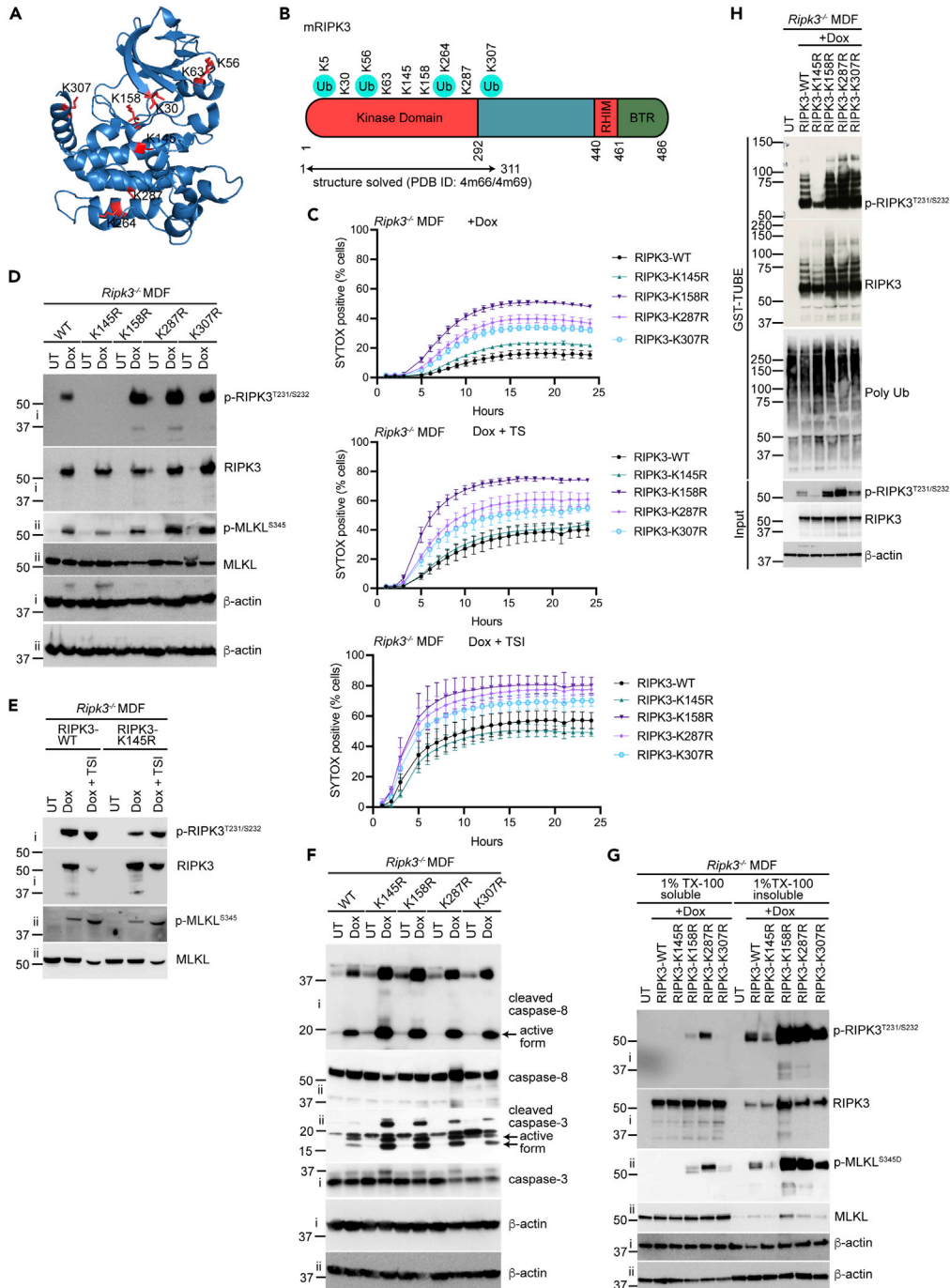
Figure 5. Surface-exposed K158, K287, and K307 of murine RIPK3 limit its cell death-inducing activity

(A) Structure of the murine RIPK3 kinase domain (PDB ID: 4M69 (Xie et al., 2013)) showing 8 conserved surface-exposed lysine residues; K30, K56, K63, K145, K158, K264, K287 and K307.

(B) Domain architecture of mouse RIPK3 depicting 4 published ubiquitylation sites (K5, K56, K264, and K307) and 5 other conserved surfaced-exposed lysine residues.

(C) *Ripk3*^{−/−} MDFs containing stably integrated dox-inducible RIPK3-WT,-K145R,-K158R,-K287R,-K307R were induced with 10 ng/mL dox and the apoptotic (TS) or necroptotic (TSI) stimuli, as indicated. Cells were monitored for viability over 24 h by SYTOX Green dye incorporation using the IncuCyte imaging system. The apoptotic stimuli consisted of 100 ng/mL TNF (T) combined with 1 μM Cp.A (S) (denoted as TS), while the necroptotic stimuli included 5 μM IDN (I) in addition to TS

Figure 5. *Continued*

(denoted TSI). Results are represented as mean±SEM of 3-5 independent experiments. See Figure S6A for the untreated cell viability controls.

(D–H) $Ripk3^{-/-}$ MDFs carrying RIPK3-WT,-K145R,-K158R,-K287R,-K307R, or-K469R were treated with 10 ng/mL (H) or 20 ng/mL dox (D–G) for 16–18 h and total cell lysates analyzed by western blotting. Roman numerals to the left of blots (i and ii) indicate the membrane probed for samples run in duplicate. In some cases, before western blotting, lysates were separated into 1% TX-100-soluble or-insoluble fractions (G), or GST-TUBE pull-down was performed (H). All results are representative of 3 independent experiments. See also Figures S5 and S6.

neutrophils, and eosinophils were similar to $Ripk3^{+/+}$ animals (Figures 4K–4O). These data suggest that RIPK3-K469 ubiquitylation is required for efficient clearance of *Salmonella in vivo*, resulting in a heightened adaptive immune response.

RIPK3 residues K158, K287 and K307 restrict cell death in a similar manner to K469

The normal RIPK3-induced cell death responses in $Ripk3^{K469R/K469R}$ macrophages and fibroblasts suggested that other RIPK3 lysine residues and ubiquitylation sites might compensate for the loss of RIPK3-K469 ubiquitylation to restrain RIPK3 activity. Analysis of the mouse RIPK3 crystal structure, which incorporates only the kinase domain (Xie et al., 2013), revealed that there are 8 surface-exposed lysine residues that might be targeted for additional ubiquitin modifications (Figure 5A). Sequence alignment of these RIPK3 lysine residues revealed that they were conserved across different species (Figure S5A). Three of these lysines, K56, K264 and K307, in addition to K5, have been reported as being modified with ubiquitin to impact RIPK3 by (1) targeting it for proteasomal (K264) or lysosomal (K56) turnover, (2) increasing RIPK1/RIPK3 complex formation (K5), or (3) limiting RIPK1/RIPK3 complex formation (K307) (Lee et al., 2019; Moriwaki and Chan, 2016; Onizawa et al., 2015; Seo et al., 2016) (Figure 5B).

To examine the functional impact of these surface-exposed lysine residues on RIPK3, we generated a series of FLAG-tagged lysine to arginine RIPK3 substitution mutants, including published ubiquitylated lysines (Figure 5B). All 9 RIPK3 mutants were used to reconstitute $Ripk3^{-/-}$ MDFs and their expression levels were found to be comparable upon dox-induced expression, with the exception of RIPK3-K307R which, relative to RIPK3-WT, displayed moderately elevated levels when induced with 5 ng/mL, but not 20 ng/mL, of dox (Figure S5B).

To test mutant RIPK3 killing activity, the RIPK3 lysine to arginine variants were treated with increasing doses of dox, and subsequent cell death measured after 16 h by PI uptake and quantified by flow cytometry, and long-term viability assessed using clonogenic survival assays. RIPK3-K56R, -K63R, and -K264R expression all induced a moderate increase in cell death compared to RIPK3-WT in the long (but not short) term analysis whereas RIPK3-K158R, -K287R, and -K307R resulted in markedly enhanced cell death following both overnight dox treatment and in long term clonogenic survival assays (Figures S5C–S5E). Although RIPK3-K5R, RIPK3-K30R and -K145R could accelerate cell death, this effect was not consistently observed when these variants were expressed in $Ripk3^{-/-}$ MDF cell lines derived from independent mice (Figures S5C and S5D).

Next, we used the IncuCyte imaging system to assess the real-time cell death kinetics of RIPK3-K145R, K158R, -K287R, and -K307R variants by SYTOX dye incorporation. Increased cell death was observed in cells expressing RIPK3-K158R, -K287R, and -K307R, either on dox induction alone, or upon RIPK3-mediated TS-induced apoptosis or TSI-induced necroptosis (Figures 5C, S4A, and S6A). On the other hand, RIPK3-K145R did not impact TSI-mediated necroptosis or TS-induced apoptosis when compared to RIPK3-WT, even though it displayed a minor increase in cell death caused by dox treatment alone (Figure 5C).

Consistent with increased necroptotic cell death signaling, expression of RIPK3-K158R, K287R, and RIPK3-K307R led to enhanced p-RIPK3$^{T231/S232}$ and p-MLKL^{S345} (Figure 5D). Reminiscent of RIPK3-K469R expression, these mutations also caused spontaneous p-RIPK3$^{T231/S232}$ within 4–6 h before the detection of cell death (Figures S6B and S6C). Moreover, in line with the observed increase in RIPK3-driven apoptosis, RIPK3-K158R, -K287R, and -K307R expression resulted in increased caspase-8 and -3 processing when compared to the levels observed in RIPK3-WT-expressing cells (Figure 5F). When expressed in $Ripk3^{-/-}$ MDF clone #2, RIPK3-K145R also increased cleavage of caspase-8 and caspase-3 (Figure 5F), in line with its ability to modestly induce cell death (Figure S5D).
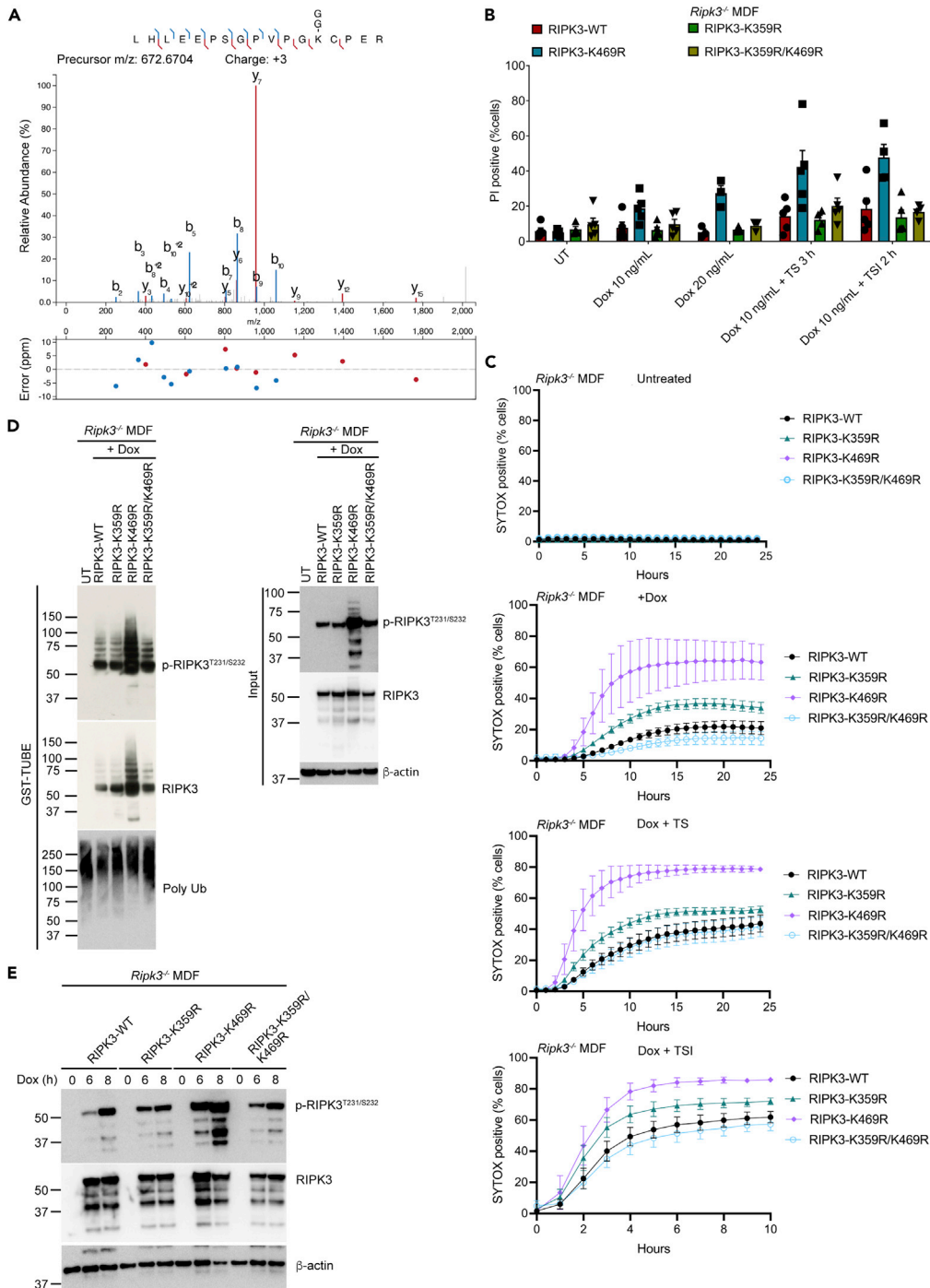
Figure 6. Loss of RIPK3-K359 ubiquitin modification prevents increased RIPK3-K469R killing activity

(A) *Ripk3*^{−/−} MDFs containing stably integrated dox-inducible RIPK3-WT or RIPK3-K469R were treated with 20 ng/mL dox for 16–18 h and FLAG-RIPK3 purified, digested with trypsin and analysis by mass spectrometry for diGly motifs present in mutant RIPK3-K469R but not RIPK3-WT. LC-MS/MS spectra of a diGly motif on K359 that was identified on FLAG-purified RIPK3-K469R but not RIPK3-WT.

(B–D) *Ripk3*^{−/−} MDFs containing stably integrated dox-inducible RIPK3-WT, -K359R, -K469R, and -K359R/K469R were treated with dox at the indicated concentration for 16–18 h prior to PI analysis by flow cytometry (B), with 10 ng/mL dox and analysis of cell death by IncuCyte Imaging (C), or with 20 ng/mL dox and analysis via GST-TUBE purification (D). Where indicated, cells were also treated with 100 ng/mL TNF (T) and 1 μM Cp.A (S) to induce apoptosis (TS), or TS combined with

Figure 6. Continued

5 μM IDN (I) (TSI) to induce necroptosis for the duration of the experiment. For flow cytometry experiments, TS and TSI were added after dox stimulation for 16–18 h (B), whereas for real-time IncuCyte imaging analysis, TS and TSI were added at the same time as dox (C). All results are depicted as mean ± SEM of 3–5 independent experiments (B) or 3 experiments (C), or representative of 3 independent experiments (D).

(E) Western blot analysis of $Ripk3^{-/-}$ MDFs expressing the indicated RIPK3 variants (10 ng/mL dox treatement). Results are representative of 3 independent experiments. See also Figure S6.

Similar to RIPK3-K469R, expression of hyperactive RIPK3-K158R, RIPK3-K287R, and RIPK3-K307R in $Ripk3^{-/-}$ MDFs also caused enhanced migration of active RIPK3 into the TX-100-insoluble fraction alongside activated MLKL (Figure 5G). Increased RIPK3 activation (as detected by T231/S232 phosphorylation) and killing activity of RIPK3-K158R, RIPK3-K287R, and RIPK3-K307R also correlated with enhanced RIPK3 ubiquitylation when compared to RIPK3-WT, including ubiquitylation of phosphorylated RIPK3 (Figure 5H). In contrast, expression of RIPK3-K145R, which does not increase RIPK3-induced necroptosis signaling (Figures 5C–5E), did not result in increased ubiquitylation when compared to RIPK3-WT (Figure 5H). Therefore, several surface-exposed and/or ubiquitylated RIPK3 lysine residues, namely K158, K287 and K307, can restrict RIPK3-induced apoptosis and necroptosis signaling upon dox-induced expression, akin to RIPK3-K469. The decoration of these sites by ubiquitin may compensate for the loss of RIPK3-K469 ubiquitylation in $Ripk3^{K469R/K469R}$ macrophages and fibroblasts to restrain RIPK3 killing activity.

RIPK3-K469 ubiquitylation can restrict cell death by preventing upstream ubiquitylation on K359

Because the loss of RIPK3-K469 ubiquitylation enhanced overall RIPK3 ubiquitylation and cell death, we hypothesized that RIPK3-K469 ubiquitylation is required to prevent the ubiquitylation of RIPK3 on other residues, which consequently trigger RIPK3 signaling. Therefore, we performed mass spectrometry directly comparing RIPK3-WT and RIPK3-K469R modification on dox-induced expression in $Ripk3^{-/-}$ MDFs. This analysis revealed a new ubiquitylation site, RIPK3-K359, that was only detected on RIPK3-K469R (Figure 6A). Sequence alignment of RIPK3 demonstrated that RIPK3-K359 is highly conserved (Figure S6D).

To assess the significance of RIPK3-K359 ubiquitylation, we generated a RIPK3-K359R mutant alone and in combination with the RIPK3-K469R mutation, RIPK3-K359R/K469R. Introduction of the RIPK3-K359R mutation on top of RIPK3-K469R was sufficient to limit increased RIPK3-K469R-triggered cell death, including death resulting from dox treatment alone or in combination with TS or TSI stimulation to trigger apoptosis or necroptosis, respectively (Figures 6B and 6C). Of note, TS- and TSI-induced RIPK3-mediated apoptosis and necroptosis was not defective in RIPK3-K359R-expressing cells when compared to RIPK3-WT (Figures 6B, 6C, and S6E), indicating that the decoration of RIPK3-K359 by ubiquitin is not universally required for RIPK3 signaling.

We next assessed the level of RIPK3 ubiquitylation by TUBE purification of the ubiquitylated proteome. Consistent with the level of RIPK3 ubiquitylation correlating with its activation, the reduced cell death observed in RIPK3-K359R/K469R-expressing cells correlated with a reduction in the total ubiquitylation of both p-RIPK3$^{T231/S232}$ and RIPK3 to a level that was similar to RIPK3-WT-expressing cells (Figure 6D). In agreement with this, a dox time-course analysis over 8 h showed delayed p-RIPK3$^{T231/S232}$ in RIPK3-K359R/K469R-expressing cells relative to RIPK3-K469R (Figure 6E). Therefore, RIPK3-K469 ubiquitylation may prevent increased cell death signaling by inhibiting ubiquitin conjugation onto RIPK3-K359.

We hypothesized that, in addition to RIPK3-K469, other inhibitory lysines may prevent increased RIPK3 activity by suppressing RIPK3-K359 ubiquitylation. To test this idea, we generated a RIPK3-K158R/K359R double mutant to compare to RIPK3-K158R expression, which functions similarly to RIPK3-K469R to increase RIPK3-mediated cell death when overexpressed (Figure 5). Similar to RIPK3-K359R/K469R (Figure 6E), RIPK3-K158R/K359R phosphorylation was delayed when compared to RIPK3-K158R (Figure 7A), which translated to reduced p-MLKL^{S345} (Figure 7B), cell death (mostly apoptotic; Figures 7C, 7D, and S6E) and overall ubiquitylated levels of p-RIPK3$^{T231/S232}$ and RIPK3 (Figure 7E). Immunoprecipitation of FLAG-RIPK3 revealed that the ability of RIPK3-K158R and RIPK3-K469R to bind activated MLKL was also decreased upon the loss of RIPK3-K359 ubiquitylation (Figure 7F). Altogether, these data suggest that RIPK3-K359 ubiquitylation is inhbited by the ubiquitylation of other RIPK3 lysine residues, and that the decoration of RIPK3-K359 with ubiquitin may act to promote RIPK3-induced cell death in some circumstances (Figure S6F).
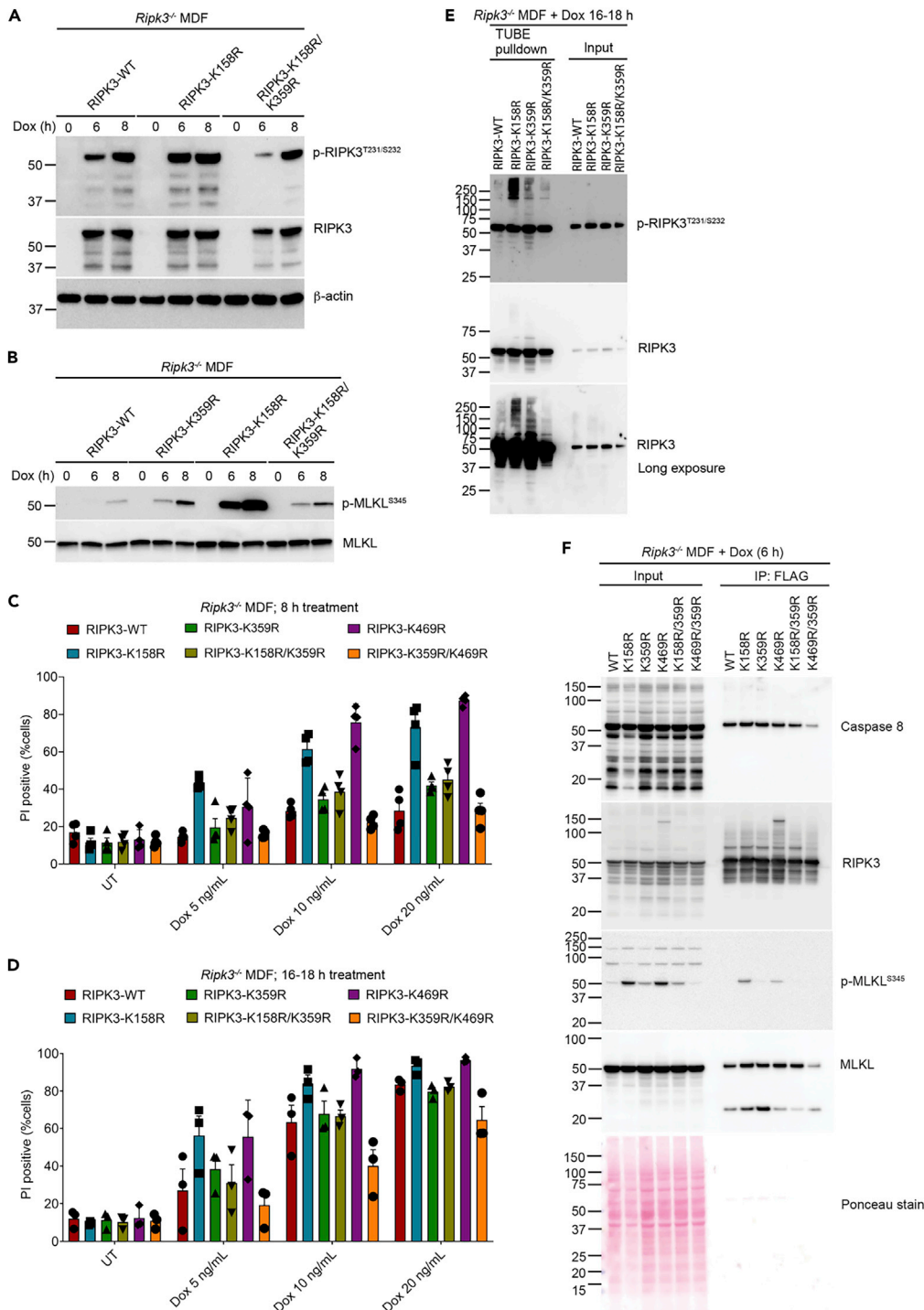
Figure 7. Loss of RIPK3-K359 ubiquitin modification limits increased RIPK3 activity resulting from RIPK3-K158R expression

(A–F) *Ripk3*$^{−/−}$ MDFs containing stably integrated dox-inducible RIPK3-WT, -K158R, -K359R, -K469R, -K158R/K359R, and -K359R/K469R were treated with 10 ng/mL dox for the indicated times before western blot analysis (A and B), GST-TUBE pull-down (E) or FLAG immunoprecipitation (F). Alternatively, cells were treated at varying concentrations of dox for 8 or 16 h before PI analysis by flow cytometry (C and D).Data are representative of 2 (F) or 3 independent experiments (A, B, and E), or depicted as mean ± SEM of 3–4 independent experiments (C and D, symbols). See also Figure S6.

DISCUSSION

Our work demonstrates that murine RIPK3 is decorated by ubiquitin 8 amino acids beyond-the-RHIM (BTR) on lysine 469. *In vitro*, the mutation of RIPK3 lysine 469 to arginine revealed that RIPK3-K469 ubiquitylation can act to limit RIPK3-driven cell death. Enhanced RIPK3-K469R-mediated cell death was conferred, in part, by the triggering of ubiquitylation on RIPK3-K359. Hence, inhibitory ubiquitylation of RIPK3 BTR may act to prevent ubiquitin being attached to alternate lysine residues that otherwise contribute to RIPK3 activation. Cell death caused by the loss of RIPK3-K469 ubiquitylation included features of both apoptosis as well as necroptosis, which likely resulted from the increased propensity of RIPK3-K469R to oligomerize when over-expressed, resulting in both its autophosphorylation and MLKL activation, in addition to the recruitment and activation of apoptotic caspase-8.

A threshold level of RIPK3 expression seems to be important to reveal the RIPK3-K469R phenotype, which is readily observed upon doxycycline-induced overexpression. Consistent with this, via the generation of *Ripk3*$^{K469R/K469R}$ mice, we showed that at steady-state endogenous levels, RIPK3-K469R had no impact on macrophage or fibroblast death caused by apoptotic (TS) or necroptotic (TSI) inducing agents. In this regard, in response to these stimuli, our data suggest that other ubiquitylation sites may act in place of, or in a co-operative manner with, RIPK3-K469 ubiquitylation to prevent the formation of a hyper-ubiquitylated RIPK3 species that signals cell death. This idea is consistent with studies showing that several RIPK3 ubiquitylation sites act to enhance RIPK3-induced cell death when mutated (Lee et al., 2019; Roedig et al., 2021; Seo et al., 2016), and our data demonstrating that both endogenous and over-expressed mutant RIPK3 killing efficiency correlates with increased levels of ubiquitylated RIPK3. It is interesting to note that the ubiquitylation of other necrosome or ripoptosome components, including RIPK1 (deAlmagro et al., 2017), MLKL (Garcia et al., 2021; Liu et al., 2021) and caspase-8 (Jin et al., 2009), can also act to promote their cell death signaling activity. Although murine RIPK3 K469 is not conserved in human RIPK3, human RIPK3 has been reported to be ubiquitylated beyond the RHIM at lysine 518, and mutation of this residue to arginine, akin to murine RIPK3 K469R, also enhanced RIPK3 killing activity (Roedig et al., 2021). Therefore, the ubiquitylation of the cell death machinery appears to be a conserved mechanism that controls their signaling, with site-specific modifications limiting cell death activity, and others promoting it, perhaps via increasing the tendency of cell death components to oligomerize.

Upon doxycycline treatment, RIPK3-K469R expression was often observed to be moderately elevated relative to RIPK3-WT, as detected by immunoblot. However, this alone is unlikely to explain the significantly increased cell death of RIPK3-K469R expressing cells. First, our analysis of other RIPK3 surface exposed or ubiquitylated lysines identified three other residues (K158, K287, K307) that also cause increased RIPK3 activation and cell death when mutated to arginine. In all cases, including RIPK3-K469R, the exacerbated RIPK3 activation (i.e. phosphorylation) did not correlate with a corresponding equivalent increase in total RIPK3 levels. Consistent with this, our mass-spectrometry analysis indicated that RIPK3-K469R phosphorylation was increased ~16–32-fold relative to RIPK3-WT, in agreement with our quantitative confocal single cell analysis of RIPK3 levels and activation. Second, other surface-exposed lysines such as RIPK3 K145, which did not enhance RIPK3 activity when mutated to arginine, showed very similar RIPK3 expression levels to activating RIPK3 variants.

The higher *Salmonella* burdens we observed on infection of *Ripk3*$^{K469R/K469R}$ mice could reflect a stimulus that increases RIPK3-K469R levels and/or allows for enhanced RIPK3-K469R killing activity in a cell type required for controlling bacterial replication. This idea aligns with our observations showing that *Salmonella*-infected *Ripk3*$^{K469R/K469R}$ mice have decreased levels of the anti-microbial cytokine IFNγ despite elevated lymphocyte numbers. However, to date, we do not know which cell type is impacted by RIPK3-K469R expression to allow for increased bacterial burdens, particularly as macrophages derived from *Ripk3*$^{K469R/K469R}$ mice displayed normal cell death responses to *Salmonella* infection *in vitro*. As previously reported (Pobezinskaya et al., 2008), TNF and TLR signaling components can function in an exqusitely cell type-specific manner and, therefore, defining the relevant cell type impacted by RIPK3 K469R expression that helps control *Salmonella* replication will be of interest to determine.

Contrary to several RIPK3 ubiquitylation studies to date (Choi et al., 2018; Lee et al., 2019; Moriwaki and Chan, 2016; Onizawa et al., 2015; Roedig et al., 2021; Seo et al., 2016), we observed that the loss of a

RIPK3 ubiquitylation site does not always result in a reduction in total RIPK3 ubiquitylation levels. In fact, our results demonstrate that the loss of RIPK3 ubiquitylation at K469, or other reported ubiquitylated and/or surface-exposed lysine residues that restrict cell death, triggered a substantial increase in the detection of ubiquitylated RIPK3 species. Because the RIPK3 RHIM is required for oligomerization of RIPK3 to promote its kinase activation (Li et al., 2012), we suggest that inhibitory RIPK3 ubiquitylation serves to keep the RIPK3 RHIM in an inactive confirmation by preventing its exposure and hence propensity to form oligomers. A recent study reported that the flanking regions of the RIPK3 RHIM contribute to the RHIM structure and are indispensable for functional necrosome signaling (Wu et al., 2021). Therefore, it is possible that inhibitory RIPK3 ubiquitylation disrupts the structural integrity of the flanking regions to limit RHIM signaling.

Interestingly, mutation of RIPK3-K469 to arginine led to increased RIPK3 activation and killing activity that was attributable, in part, to the ubiquitylation of RIPK3-K359. Although RIPK3-K469 is not conserved in human RIPK3, RIPK3-K359 is highly conserved across species. Although our findings show that loss of RIPK3-K359 ubiquitylation alone does not block RIPK3-induced cell death in response to commonly used RIPK3 activating agents (i.e. TSI), the fact that the loss of RIPK3-K359 ubiquitylation diminished the cell death-inducing activity of overexpressed RIPK3-K469R implies that the ubiquitin targeting of RIPK3-K359 may act as a RIPK3 activation mechanism in response to specific stimuli.

Why a number of lysine residues located in distinct RIPK3 domains can all limit RIPK3 killing at an individual level *in vitro*, as our and other studies show, remains unclear. However, our findings highlight that data derived from the complementation of gene deficient cells (e.g. $Ripk3^{-/-}$) *in vitro* with relevant, inducibly expressed, mutant genes should be interpreted with caution, as the same responses may not be observed in all cell types and tissues in corresponding knockin gene mutant animals, as our analysis of $Ripk3^{K469R/K469R}$ mice demonstrates. As some reports suggest (Choi et al., 2018; Lee et al., 2019; Seo et al., 2016), it is possible that each currently identified RIPK3 ubiquitylation site is targeted by specific E3 ligases, or DUBs, that are inactivated/activated in response to distinct signals in a cell type specific manner, thereby allowing RIPK3 activity to be toggled according to different cellular threats. Further study and identification of E3 ligases required for the ubiquitylation of RIPK3, to either promote or limit RIPK3 signaling, may present new therapeutic avenues for modulating RIPK3 activity in relevant disease states.

Limitations of the study

Despite the retention of a positive charge, the substitution of lysine for arginine may alter the confirmation of a protein to impact its function, as indicated by previous research (Sokalingam et al., 2012). Therefore, although our mass-spectrometry analysis clearly identified the decoration of RIPK3-K469 with ubiquitin and, in the RIPK3-K469R variant, ubiquitin modification of RIPK3-K359, we cannot exclude the possibility that the lysine to arginine substitutions of these residues alters RIPK3 conformation and function independent of ubiquitin modification. In this regard, two of the surface exposed RIPK3 lysines we examined, RIPK3-K158 and RIPK3-K287, have yet to be shown as sites for ubiquitylation, yet the substitution of these residues with arginine still resulted in hyperactive RIPK3. Although our findings also indicate that increased overall RIPK3 ubiquitylation correlates with the cell death signaling of both endogenous and hyperactive mutant RIPK3, future efforts to identify the ubiquitylation fingerprint, including the ubiquitin linkage types, of endogenous RIPK3 at steady state and during necroptosis, will be important to examine. Our study also does not assess how the numerous RIPK3 residues phosphorylated upon RIPK3-K469R expression might alter RIPK3 function, and if these events result from RIPK3 kinase activity. Finally, despite the mildly reduced *Salmonella* clearance of infected $Ripk3^{K469R/K469R}$ mice, our work has not identified the relevant cell types impacted by this RIPK3 variant that alter cell death signaling or potentially other functions, such as autophagy induced by bacterial infection. Ultimately, these investigations will be required to determine the *in vivo* physiological relevance and signaling imparted by RIPK3-K469 ubiquitylation.

STAR★METHODS

Detailed methods are provided in the online version of this paper and include the following:

- KEY RESOURCES TABLE
- RESOURCE AVAILABILITY
  - Lead contact

SUPPLEMENTAL INFORMATION

Supplemental information can be found online at https://doi.org/10.1016/j.isci.2022.104632.

AUTHOR CONTRIBUTIONS

The project was conceived by DF and JEV; the experiments were designed by DF, SEG, AJK, MJH, JEV; the experiments were performed and analyzed by DF, SEG, JJS, AW, LL, ALS, MR, HA, KEL, NL, RLA, VVE, GE, JSP; expert advice and reagents were provided by EC, LM, SAC, SRS, MD, HA, AJK, MJH, RF, KEL, NL, JMM; the manuscript written by DF and JEV. All authors assisted with manuscript editing.

DECLARATION OF INTERESTS

J.M.M. and A.L.S. contribute to a project developing necroptosis inhibitors in collaboration with Anaxis Pharma.

INCLUSION AND DIVERSITY

One or more of the authors of this paper self-identifies as a member of the LGBTQ+ community. One or more of the authors of this paper self-identifies as living with a disability.

REFERENCES

Ali, M., and Mocarski, E.S. (2018). Proteasome inhibition blocks necroptosis by attenuating death complex aggregation. Cell Death Dis. 9, 346. https://doi.org/10.1038/s41419-018-0371-x.

Amrhein, V., Greenland, S., and McShane, B. (2019). Scientists rise up against statistical significance. Nature 567, 305–307. https://doi.org/10.1038/d41586-019-00857-9.

Békés, M., Prudden, J., Srikumar, T., Raught, B., Boddy, M.N., and Salvesen, G.S. (2011). The dynamics and mechanism of SUMO chain deconjugation by SUMO-specific proteases. J. Biol. Chem. 286, 10238–10247. https://doi.org/10.1074/jbc.m110.205153.

Benoun, J.M., Peres, N.G., Wang, N., Pham, O.H., Rudisill, V.L., Fogassy, Z.N., Whitney, P.G., Fernandez-Ruiz, D., Gebhardt, T., Pham, Q.M., et al. (2018). Optimal protection against Salmonella infection requires noncirculating memory. Proc. Natl. Acad. Sci. USA 115, 10416–10421. https://doi.org/10.1073/pnas.1808339115.

Bossen, C., Ingold, K., Tardivel, A., Bodmer, J.L., Gaide, O., Hertig, S., Ambrose, C., Tschopp, J., and Schneider, P. (2006). Interactions of tumor necrosis factor (TNF) and TNF receptor family members in the mouse and human. J. Biol. Chem. 281, 13964–13971. https://doi.org/10.1074/jbc.m601553200.

Chen, W., Zhou, Z., Li, L., Zhong, C.Q., Zheng, X., Wu, X., Zhang, Y., Ma, H., Huang, D., Li, W., et al. (2013). Diverse sequence determinants control human and mouse receptor interacting protein 3 (RIP3) and mixed lineage kinase domain-like (MLKL) interaction in necroptotic signaling. J. Biol. Chem. 288, 16247–16261. https://doi.org/10.1074/jbc.m112.435545.

Cho, Y.S., Challa, S., Moquin, D., Genga, R., Ray, T.D., Guildford, M., Chan, F.K.M., and Chan, F.K. (2009). Phosphorylation-driven assembly of the RIP1-RIP3 complex regulates programmed necrosis and virus-induced inflammation. Cell 137, 1112–1123. https://doi.org/10.1016/j.cell.2009.05.037.

Choi, S.W., Park, H.H., Kim, S., Chung, J.M., Noh, H.J., Kim, S.K., Song, H.K., Lee, C.W., Morgan, M.J., Kang, H.C., and Kim, Y.S. (2018). PELI1 selectively targets kinase-active RIP3 for ubiquitylation-dependent proteasomal degradation. Mol. Cell 70, 920–935.e7. https://doi.org/10.1016/j.molcel.2018.05.016.

Conos, S.A., Chen, K.W., De Nardo, D., Hara, H., Whitehead, L., Nunez, G., Masters, S.L., Murphy, J.M., Schroder, K., Vaux, D.L., et al. (2017). Active MLKL triggers the NLRP3 inflammasome in a cell-intrinsic manner. Proc. Natl. Acad. Sci. USA 114, E961–E969. https://doi.org/10.1073/pnas.1613305114.

de Almagro, M.C., Goncharov, T., Izrael-Tomasevic, A., Duttler, S., Kist, M., Varfolomeev, E., Wu, X., Lee, W.P., Murray, J., Webster, J.D., et al. (2017). Coordinated ubiquitination and phosphorylation of RIP1 regulates necroptotic cell death. Cell Death Differ. 24, 26–37. https://doi.org/10.1038/cdd.2016.78.

Doerflinger, M., Deng, Y., Whitney, P., Salvamoser, R., Engel, S., Kueh, A.J., Tai, L., Bachem, A., Gressier, E., Geoghegan, N.D., et al. (2020). Flexible usage and interconnectivity of diverse cell death pathways protect against intracellular infection. Immunity 53, 533–547.e7. https://doi.org/10.1016/j.immuni.2020.07.004.

Dondelinger, Y., Declercq, W., Montessuit, S., Roelandt, R., Goncalves, A., Bruggeman, I., Hulpiau, P., Weber, K., Sehon, C.A., Marquis, R.W., et al. (2014). MLKL compromises plasma membrane integrity by binding to phosphatidylinositol phosphates. Cell Rep. 7, 971–981. https://doi.org/10.1016/j.celrep.2014.04.026.

Dong, K., Zhu, Y., Deng, Q., Sun, L., Yang, S., Huang, K., Cao, Y., Li, Y., Wu, S., and Huang, R. (2022). Salmonella pSLT-encoded effector SpvB promotes RIPK3-dependent necroptosis in intestinal epithelial cells. Cell Death Discov. 8, 44. https://doi.org/10.1038/s41420-022-00841-9.

Duong, B.H., Onizawa, M., Oses-Prieto, J.A., Advincula, R., Burlingame, A., Malynn, B.A., and Ma, A. (2015). A20 restricts ubiquitination of pro-interleukin-1β protein complexes and suppresses NLRP3 inflammasome activity. Immunity 42, 55–67. https://doi.org/10.1016/j.immuni.2014.12.031.

Feoktistova, M., Geserick, P., Kellert, B., Dimitrova, D.P., Langlais, C., Hupe, M., Cain, K., MacFarlane, M., Häcker, G., Hacker, G., and Leverkus, M. (2011). cIAPs block Ripoptosome formation, a RIP1/caspase-8 containing intracellular cell death complex differentially regulated by cFLIP isoforms. Mol. Cell 43, 449–463. https://doi.org/10.1016/j.molcel.2011.06.011.

Franken, N.A.P., Rodermond, H.M., Stap, J., Haveman, J., and van Bree, C. (2006). Clonogenic assay of cells in vitro. Nat. Protoc. 1, 2315–2319. https://doi.org/10.1038/nprot.2006.339.

Galluzzi, L., Kepp, O., Chan, F.K.M., and Kroemer, G. (2017). Necroptosis: mechanisms and relevance to disease. Annu. Rev. Pathol. 12, 103–130. https://doi.org/10.1146/annurev-pathol-052016-100247.

Garcia, L.R., Tenev, T., Newman, R., Haich, R.O., Liccardi, G., John, S.W., Annibaldi, A., Yu, L., Pardo, M., Young, S.N., et al. (2021). Ubiquitylation of MLKL at lysine 219 positively regulates necroptosis-induced tissue injury and pathogen clearance. Nat. Commun. 12, 3364. https://doi.org/10.1038/s41467-021-23474-5.

Garnish, S.E., Meng, Y., Koide, A., Sandow, J.J., Denbaum, E., Jacobsen, A.V., Yeung, W., Samson, A.L., Horne, C.R., Fitzgibbon, C., et al. (2021). Conformational interconversion of MLKL and disengagement from RIPK3 precede cell death by necroptosis. Nat. Commun. 12, 2211. https://doi.org/10.1038/s41467-021-22400-z.

Giogha, C., and Lawlor, K.E. (2019). Sugar fix keeps RIPK3 at bay. Immunity 50, 539–541. https://doi.org/10.1016/j.immuni.2019.02.018.

He, S., Liang, Y., Shao, F., and Wang, X. (2011). Toll-like receptors activate programmed necrosis in macrophages through a receptor-interacting kinase-3-mediated pathway. Proc. Natl. Acad. Sci. USA 108, 20054–20059. https://doi.org/10.1073/pnas.1116302108.

He, S., Wang, L., Miao, L., Wang, T., Du, F., Zhao, L., and Wang, X. (2009). Receptor interacting protein kinase-3 determines cellular necrotic response to TNF-α. Cell 137, 1100–1111. https://doi.org/10.1016/j.cell.2009.05.021.

Heckman, K.L., and Pease, L.R. (2007). Gene splicing and mutagenesis by PCR-driven overlap extension. Nat. Protoc. 2, 924–932. https://doi.org/10.1038/nprot.2007.132.

Hildebrand, J.M., Tanzer, M.C., Lucet, I.S., Young, S.N., Spall, S.K., Sharma, P., Pierotti, C., Garnier, J.M., Dobson, R.C.J., Webb, A.I., et al. (2014). Activation of the pseudokinase MLKL unleashes the four-helix bundle domain to induce membrane localization and necroptotic cell death. Proc. Natl. Acad. Sci. USA 111, 15072–15077. https://doi.org/10.1073/pnas.1408987111.

Hjerpe, R., Aillet, F., Lopitz-Otsoa, F., Lang, V., England, P., and Rodriguez, M.S. (2009). Efficient protection and isolation of ubiquitylated proteins using tandem ubiquitin-binding entities. EMBO Rep. 10, 1250–1258. https://doi.org/10.1038/embor.2009.192.

Jin, Z., Li, Y., Pitti, R., Lawrence, D., Pham, V.C., Lill, J.R., and Ashkenazi, A. (2009). Cullin3-based polyubiquitination and p62-dependent aggregation of caspase-8 mediate extrinsic apoptosis signaling. Cell 137, 672–684. https://doi.org/10.1016/s9999-9994(09)00534-0.

Kaiser, W.J., Sridharan, H., Huang, C., Mandal, P., Upton, J.W., Gough, P.J., Sehon, C.A., Marquis, R.W., Bertin, J., and Mocarski, E.S. (2013). Toll-like receptor 3-mediated necrosis via TRIF, RIP3, and MLKL. J. Biol. Chem. 288, 31268–31279. https://doi.org/10.1074/jbc.m113.462341.

Kamitani, T., Nguyen, H.P., Kito, K., Fukuda-Kamitani, T., and Yeh, E.T. (1998). Covalent modification of PML by the sentrin family of ubiquitin-like proteins. J. Biol. Chem. 273, 3117–3120. https://doi.org/10.1074/jbc.273.6.3117.

Kang, T.B., Yang, S.H., Toth, B., Kovalenko, A., and Wallach, D. (2013). Caspase-8 blocks kinase RIPK3-mediated activation of the NLRP3 inflammasome. Immunity 38, 27–40. https://doi.org/10.1016/j.immuni.2012.09.015.

Kupz, A., Bedoui, S., and Strugnell, R.A. (2014). Cellular requirements for systemic control of Salmonella enterica serovar Typhimurium infections in mice. Infect. Immun. *82*, 4997–5004. https://doi.org/10.1128/iai.02192-14.

Lalaoui, N., Boyden, S.E., Oda, H., Wood, G.M., Stone, D.L., Chau, D., Liu, L., Stoffels, M., Kratina, T., Lawlor, K.E., et al. (2020). Mutations that prevent caspase cleavage of RIPK1 cause auto-inflammatory disease. Nature *577*, 103–108. https://doi.org/10.1038/s41586-019-1828-5.

Lawlor, K.E., Feltham, R., Yabal, M., Conos, S.A., Chen, K.W., Ziehe, S., Graß, C., Zhan, Y., Nguyen, T.A., Hall, C., et al. (2017). XIAP loss triggers RIPK3- and caspase-8-driven IL-1β activation and cell death as a consequence of TLR-MyD88-induced cIAP1-TRAF2 degradation. Cell Rep. *20*, 668–682. https://doi.org/10.1016/j.celrep.2017.06.073.

Lawlor, K.E., Khan, N., Mildenhall, A., Gerlic, M., Croker, B.A., D'Cruz, A.A., Hall, C., Kaur Spall, S., Anderton, H., Masters, S.L., et al. (2015). RIPK3 promotes cell death and NLRP3 inflammasome activation in the absence of MLKL. Nat. Commun. *6*, 6282. https://doi.org/10.1038/ncomms7282.

Lee, S.B., Kim, J.J., Han, S.A., Fan, Y., Guo, L.S., Aziz, K., Nowsheen, S., Kim, S.S., Park, S.Y., Luo, Q., et al. (2019). The AMPK-Parkin axis negatively regulates necroptosis and tumorigenesis by inhibiting the necrosome. Nat. Cell Biol. *21*, 940–951. https://doi.org/10.1038/s41556-019-0356-8.

Li, J., McQuade, T., Siemer, A.B., Napetschnig, J., Moriwaki, K., Hsiao, Y.S., Damko, E., Moquin, D., Walz, T., McDermott, A., et al. (2012). The RIP1/RIP3 necrosome forms a functional amyloid signaling complex required for programmed necrosis. Cell *150*, 339–350. https://doi.org/10.1016/j.cell.2012.06.019.

Li, X., Gong, W., Wang, H., Li, T., Attri, K.S., Lewis, R.E., Kalil, A.C., Bhinderwala, F., Powers, R., Yin, G., et al. (2019). O-GlcNAc transferase suppresses inflammation and necroptosis by targeting receptor-interacting serine/threonine-protein kinase 3. Immunity *50*, 1115. https://doi.org/10.1016/j.immuni.2019.03.008.

Lim, J., Park, H., Heisler, J., Maculins, T., Roose-Girma, M., Xu, M., McKenzie, B., van Lookeren Campagne, M., Newton, K., and Murthy, A. (2019). Autophagy regulates inflammatory programmed cell death via turnover of RHIM-domain proteins. Elife *8*, e44452. https://doi.org/10.7554/elife.44452.

Liu, Z., Dagley, L.F., Shield-Artin, K., Young, S.N., Bankovacki, A., Wang, X., Tang, M., Howitt, J., Stafford, C.A., Nachbur, U., et al. (2021). Oligomerization-driven MLKL ubiquitylation antagonizes necroptosis. EMBO J. *40*, e103718. https://doi.org/10.15252/embj.2019103718.

Mandal, P., Berger, S.B., Pillay, S., Moriwaki, K., Huang, C., Guo, H., Lich, J.D., Finger, J., Kasparcova, V., Votta, B., et al. (2014). RIP3 induces apoptosis independent of pronecrotic kinase activity. Mol. Cell *56*, 481–495. https://doi.org/10.1016/j.molcel.2014.10.021.

Meng, Y., Sandow, J.J., Czabotar, P.E., and Murphy, J.M. (2021). The regulation of necroptosis by post-translational modifications.

Cell Death Differ. *28*, 861–883. https://doi.org/10.1038/s41418-020-00722-7.

Miao, W., Qu, Z., Shi, K., Zhang, D., Zong, Y., Zhang, G., Zhang, G., and Hu, S. (2015). RIP3 S-nitrosylation contributes to cerebral ischemic neuronal injury. Brain Res. *1627*, 165–176. https://doi.org/10.1016/j.brainres.2015.08.020.

Moriwaki, K., Balaji, S., McQuade, T., Malhotra, N., Kang, J., and Chan, F.M. (2014). The necroptosis adaptor RIPK3 promotes injury-induced cytokine expression and tissue repair. Immunity *41*, 567–578. https://doi.org/10.1016/j.immuni.2014.09.016.

Moriwaki, K., and Chan, F.K.M. (2016). Regulation of RIPK3- and RHIM-dependent necroptosis by the proteasome. J. Biol. Chem. *291*, 5948–5959. https://doi.org/10.1074/jbc.m115.700997.

Moujalled, D.M., Cook, W.D., Murphy, J.M., and Vaux, D.L. (2014). Necroptosis induced by RIPK3 requires MLKL but not Drp1. Cell Death Dis. *5*, e1086. https://doi.org/10.1038/cddis.2014.18.

Moujalled, D.M., Cook, W.D., Okamoto, T., Murphy, J., Lawlor, K.E., Vince, J.E., and Vaux, D.L. (2013). TNF can activate RIPK3 and cause programmed necrosis in the absence of RIPK1. Cell Death Dis. *4*, e465. https://doi.org/10.1038/cddis.2012.201.

Müller, T., Dewitz, C., Schmitz, J., Schröder, A.S., Bräsen, J.H., Stockwell, B.R., Murphy, J.M., Kunzendorf, U., and Krautwald, S. (2017). Necroptosis and ferroptosis are alternative cell death pathways that operate in acute kidney failure. Cell. Mol. Life Sci. *74*, 3631–3645. https://doi.org/10.1007/s00018-017-2547-4.

Murai, S., Yamaguchi, Y., Shirasaki, Y., Yamagishi, M., Shindo, R., Hildebrand, J.M., Miura, R., Nakabayashi, O., Totsuka, M., Tomida, T., et al. (2018). A FRET biosensor for necroptosis uncovers two different modes of the release of DAMPs. Nat. Commun. *9*, 4457. https://doi.org/10.1038/s41467-018-06985-6.

Murphy, J.M., Czabotar, P.E., Hildebrand, J.M., Lucet, I.S., Zhang, J.G., Alvarez-Diaz, S., Lewis, R., Lalaoui, N., Metcalf, D., Webb, A.I., et al. (2013). The pseudokinase MLKL mediates necroptosis via a molecular switch mechanism. Immunity *39*, 443–453. https://doi.org/10.1016/j.immuni.2013.06.018.

Murphy, J.M., and Vince, J.E. (2015). Post-translational control of RIPK3 and MLKL mediated necroptotic cell death. F1000Research *4*, 1297. https://doi.org/10.12688/f1000research.7046.1.

Newton, K., Dugger, D.L., Maltzman, A., Greve, J.M., Hedehus, M., Martin-McNulty, B., Martin-McNulty, B., Carano, R.A., Cao, T.C., van Bruggen, N., et al. (2016a). RIPK3 deficiency or catalytically inactive RIPK1 provides greater benefit than MLKL deficiency in mouse models of inflammation and tissue injury. Cell Death Differ. *23*, 1565–1576. https://doi.org/10.1038/cdd.2016.46.

Newton, K., Dugger, D.L., Wickliffe, K.E., Kapoor, N., de Almagro, M.C., Vucic, D., Komuves, L., Ferrando, R.E., French, D.M., Webster, J., et al. (2014). Activity of protein kinase RIPK3 determines whether cells die by necroptosis or apoptosis. Science *343*, 1357–1360. https://doi.org/10.1126/science.1249361.

Newton, K., Sun, X., and Dixit, V.M. (2004). Kinase RIP3 is dispensable for normal NF-kappa Bs, signaling by the B-cell and T-cell receptors, tumor necrosis factor receptor 1, and Toll-like receptors 2 and 4. Mol. Cell. Biol. *24*, 1464–1469. https://doi.org/10.1128/mcb.24.4.1464-1469.2004.

Newton, K., Wickliffe, K.E., Maltzman, A., Dugger, D.L., Strasser, A., Pham, V.C., Lill, J.R., Roose-Girma, M., Warming, S., Solon, M., et al. (2016b). RIPK1 inhibits ZBP1-driven necroptosis during development. Nature *540*, 129–133. https://doi.org/10.1038/nature20559.

Onizawa, M., Oshima, S., Schulze-Topphoff, U., Oses-Prieto, J.A., Lu, T., Tavares, R., Prodhomme, T., Duong, B., Whang, M.I., Advincula, R., et al. (2015). The ubiquitin-modifying enzyme A20 restricts ubiquitination of the kinase RIPK3 and protects cells from necroptosis. Nat. Immunol. *16*, 618–627. https://doi.org/10.1038/ni.3172.

Orozco, S., and Oberst, A. (2017). RIPK3 in cell death and inflammation: the good, the bad, and the ugly. Immunol. Rev. *277*, 102–112. https://doi.org/10.1111/imr.12536.

Pefanis, A., Ierino, F.L., Murphy, J.M., and Cowan, P.J. (2019). Regulated necrosis in kidney ischemia-reperfusion injury. Kidney Int. *96*, 291–301. https://doi.org/10.1016/j.kint.2019.02.009.

Petrie, E.J., Sandow, J.J., Jacobsen, A.V., Smith, B.J., Griffin, M.D.W., Lucet, I.S., Dai, W., Young, S.N., Tanzer, M.C., Wardak, A., et al. (2018). Conformational switching of the pseudokinase domain promotes human MLKL tetramerization and cell death by necroptosis. Nat. Commun. *9*, 2422. https://doi.org/10.1038/s41467-018-04714-7.

Petrie, E.J., Sandow, J.J., Lehmann, W.I.L., Liang, L.Y., Coursier, D., Young, S.N., Kersten, W.J.A., Fitzgibbon, C., Samson, A.L., Jacobsen, A.V., et al. (2019). Viral MLKL homologs subvert necroptotic cell death by sequestering cellular RIPK3. Cell Rep. *28*, 3309–3319.e5. https://doi.org/10.1016/j.celrep.2019.08.055.

Pobezinskaya, Y.L., Kim, Y.S., Choksi, S., Morgan, M.J., Li, T., Liu, C., and Liu, Z. (2008). The function of TRADD in signaling through tumor necrosis factor receptor 1 and TRIF-dependent Toll-like receptors. Nat. Immunol. *9*, 1047–1054. https://doi.org/10.1038/ni.1639.

Polykratis, A., Martens, A., Eren, R.O., Shirasaki, Y., Yamagishi, M., Yamaguchi, Y., Uemura, S., Miura, M., Holzmann, B., Kollias, G., et al. (2019). A20 prevents inflammasome-dependent arthritis by inhibiting macrophage necroptosis through its ZnF7 ubiquitin-binding domain. Nat. Cell Biol. *21*, 731–742. https://doi.org/10.1038/s41556-019-0324-3.

Robinson, N., McComb, S., Mulligan, R., Dudani, R., Krishnan, L., and Sad, S. (2012). Type I interferon induces necroptosis in macrophages during infection with Salmonella enterica serovar Typhimurium. Nat. Immunol. *13*, 954–962. https://doi.org/10.1038/ni.2397.

Roedig, J., Kowald, L., Juretschke, T., Karlowitz, R., Ahangarian Abhari, B., Roedig, H., Fulda, S., Beli, P., and van Wijk, S.J. (2021). USP22 controls necroptosis by regulating receptor-interacting protein kinase 3 ubiquitination. EMBO Rep. *22*,

e50163. https://doi.org/10.15252/embr.202050163.

Samson, A.L., Garnish, S.E., Hildebrand, J.M., and Murphy, J.M. (2021). Location, location, location: a compartmentalized view of TNF-induced necroptotic signaling. Sci. Signal. 14, eabc6178. https://doi.org/10.1126/scisignal.abc6178.

Samson, A.L., Zhang, Y., Geoghegan, N.D., Gavin, X.J., Davies, K.A., Mlodzianoski, M.J., Whitehead, L.W., Frank, D., Garnish, S.E., Fitzgibbon, C., et al. (2020). MLKL trafficking and accumulation at the plasma membrane control the kinetics and threshold for necroptosis. Nat. Commun. 11, 3151. https://doi.org/10.1038/s41467-020-16887-1.

Satkovich, J., Anderson, C.J., Medina, C.B., Ottolini, M., Lukens, J.R., and Kendall, M.M. (2020). RIPK3-Dependent recruitment of low-inflammatory myeloid cells does not protect from systemic Salmonella infection. mBio 11, e02588-20. https://doi.org/10.1128/mbio.02588-20.

Seo, J., Lee, E.W., Sung, H., Seong, D., Dondelinger, Y., Shin, J., Jeong, M., Lee, H.K., Kim, J.H., Han, S.Y., et al. (2016). CHIP controls necroptosis through ubiquitylation- and lysosome-dependent degradation of RIPK3. Nat. Cell Biol. 18, 291–302. https://doi.org/10.1038/ncb3314.

Shutinoski, B., Patel, R., Tomlinson, J.J., Schlossmacher, M.G., and Sad, S. (2020). Ripk3 licenced protection against microbial infection in the absence of Caspase1-11 inflammasome. Microbes Infect. 22, 40–45. https://doi.org/10.1016/j.micinf.2019.08.002.

Silke, J., Rickard, J.A., and Gerlic, M. (2015). The diverse role of RIP kinases in necroptosis and inflammation. Nat. Immunol. 16, 689–697. https://doi.org/10.1038/ni.3206.

Sokalingam, S., Raghunathan, G., Soundrarajan, N., and Lee, S.G. (2012). A study on the effect of surface lysine to arginine mutagenesis on protein stability and structure using green fluorescent protein. PLoS One 7, e40410. https://doi.org/10.1371/journal.pone.0040410.

Strugnell, R., Dougan, G., Chatfield, S., Charles, I., Fairweather, N., Tite, J., Li, J.L., Beesley, J., and Roberts, M. (1992). Characterization of a Salmonella typhimurium aro vaccine strain expressing the P.69 antigen of Bordetella pertussis. Infect. Immun. 60, 3994–4002. https://doi.org/10.1128/iai.60.10.3994-4002.1992.

Sun, L., Wang, H., Wang, Z., He, S., Chen, S., Liao, D., Wang, L., Yan, J., Liu, W., Lei, X., and Wang, X. (2012). Mixed lineage kinase domain-like protein mediates necrosis signaling downstream of RIP3 kinase. Cell 148, 213–227. https://doi.org/10.1016/j.cell.2011.11.031.

Sun, X., Yin, J., Starovasnik, M.A., Fairbrother, W.J., and Dixit, V.M. (2002). Identification of a novel homotypic interaction motif required for the phosphorylation of receptor-interacting protein (RIP) by RIP3. J. Biol. Chem. 277, 9505–9511. https://doi.org/10.1074/jbc.m109488200.

Tenev, T., Bianchi, K., Darding, M., Broemer, M., Langlais, C., Wallberg, F., Zachariou, A., Lopez, J., MacFarlane, M., Cain, K., and Meier, P. (2011). The Ripoptosome, a signaling platform that assembles in response to genotoxic stress and loss of IAPs. Mol. Cell 43, 689. https://doi.org/10.1016/j.molcel.2011.08.005.

Upton, J.W., Kaiser, W.J., and Mocarski, E.S. (2012). DAI/ZBP1/DLM-1 complexes with RIP3 to mediate virus-induced programmed necrosis that is targeted by murine cytomegalovirus vIRA. Cell Host Microbe 11, 290–297. https://doi.org/10.1016/j.chom.2012.01.016.

Vijayaraj, S.L., Feltham, R., Rashidi, M., Frank, D., Liu, Z., Simpson, D.S., Ebert, G., Vince, A., Herold, M.J., Kueh, A., et al. (2021). The ubiquitylation of IL-1β limits its cleavage by caspase-1 and targets it for proteasomal degradation. Nat. Commun. 12, 2713. https://doi.org/10.1038/s41467-021-22979-3.

Vince, J.E., Wong, W.L., Wong, W.W., Gentle, I., Lawlor, K.E., Allam, R., O'Reilly, L., Mason, K., Gross, O., Ma, S., et al. (2012). Inhibitor of apoptosis proteins limit RIP3 kinase-dependent interleukin-1 activation. Immunity 36, 215–227. https://doi.org/10.1016/j.immuni.2012.01.012.

Wang, H., Sun, L., Su, L., Rizo, J., Liu, L., Wang, L.F., Wang, F.S., and Wang, X. (2014). Mixed lineage kinase domain-like protein MLKL causes necrotic membrane disruption upon phosphorylation by RIP3. Mol. Cell 54, 133–146. https://doi.org/10.1016/j.molcel.2014.03.003.

Wiśniewski, J.R., Zougman, A., Nagaraj, N., and Mann, M. (2009). Universal sample preparation method for proteome analysis. Nat. Methods 6, 359–362. https://doi.org/10.1038/nmeth.1322.

Wu, X.L., Hu, H., Dong, X.Q., Zhang, J., Wang, J., Schwieters, C.D., Liu, J., Wu, G.X., Li, B., Lin, J.Y., et al. (2021). The amyloid structure of mouse RIPK3 (receptor interacting protein kinase 3) in cell necroptosis. Nat. Commun. 12, 1627. https://doi.org/10.1038/s41467-021-21881-2.

Xie, T., Peng, W., Yan, C., Wu, J., Gong, X., and Shi, Y. (2013). Structural insights into RIP3-mediated necroptotic signaling. Cell Rep. 5, 70–78. https://doi.org/10.1016/j.celrep.2013.08.044.

Yabal, M., Müller, N., Adler, H., Knies, N., Groß, C., Damgaard, R.B., Kanegane, H., Ringelhan, M., Kaufmann, T., Heikenwälder, M., et al. (2014). XIAP restricts TNF- and RIP3-dependent cell death and inflammasome activation. Cell Rep. 7, 1796–1808. https://doi.org/10.1016/j.celrep.2014.05.008.

Zhang, D.W., Shao, J., Lin, J., Zhang, N., Lu, B.J., Lin, S.C., Dong, M.Q., and Han, J. (2009). RIP3, an energy metabolism regulator that switches TNF-induced cell death from apoptosis to necrosis. Science 325, 332–336. https://doi.org/10.1126/science.1172308.

STAR★METHODS

KEY RESOURCES TABLE

REAGENT or RESOURCE	SOURCE	IDENTIFIER
Antibodies		
Anti-β-actin	Sigma-Aldrich	Cat#: A1987; RRID: AB_476692; Clone: AC-15
Anti-Calreticulin	Cell Signaling Technology	Cat#: 12238; RRID: AB_2688013
Anti-Caspase-3	Cell Signaling Technology	Cat#: 9662; RRID: AB_331439
Anti-Cleaved Caspase-3 (D175)	Cell Signaling Technology	Cat#: 9579; RRID: AB_10897512
Anti-Cleaved Caspase-8 (D387)	Cell Signaling Technology	Cat#: 8592; RRID: AB_10891784
Anti-Flotilin-1	BD Transduction Laboratories	Cat#: 610821; RRID: AB_398140
Anti-GAPDH	Merck	Cat#: MAB374; RRID: AB_2107445; Clone: AC-15
Anti-GM130	BD Transduction Laboratories	Cat#: 610822; RRID: AB_398141; Clone: 35
Anti-HA	Roche	Cat#: 11867423001; RRID: AB_390918; Clone: 3F10
Anti-Lamin A/C	Santa Cruz	Cat#: sc-20681; RRID: AB_648154
Anti-LAMP-1	Santa Cruz	Cat#: sc-19992, RRID:AB_2134495
Anti-MLKL	WEHI	Clone 3H1
Anti-Mouse IgG (H + L) Secondary	Southern Biotech	Cat#: 1010-05; RRID: AB_2728714
Anti-Mouse IgG (H + L) Secondary, Alexa Fluor 594	Invitrogen	Cat#: R37121; RRID: AB_2556549
Anti-Phospho-MLKL (S345)	Abcam	Cat#: Ab 196436; RRID: AB_2687465
Anti-Phospho-MLKL (S345)	Cell Signaling Technology	Cat#: 37333; RRID: AB_ 2799112
Anti-Phospho-RIPK3 (T231/S232)	Genentech, Inc	Cat#: GEN-135-35-9
Anti-Rabbit IgG (H + L) Secondary	Southern Biotech	Cat#: 4010-05; RRID: AB_2632593
Anti-Rabbit IgG (H + L) Secondary, Alexa Fluor 488	Invitrogen	Cat#: A-11008; RRID: AB_143165
Anti-Rabbit IgG (H + L) Secondary, Alexa Fluor 647	Invitrogen	Cat#: A31573; RRID: AB_2536183
Anti-Rat IgG (H + L) Secondary	Southern Biotech	Cat#: 3010-05; RRID: AB_2795801
Anti-Rat IgG (H + L) Secondary, Alexa Fluor 594	Invitrogen	Cat#: A-11007; RRID: AB_141374
Anti-RIPK1	Cell Signaling Technology	Cat#: 3493; RRID: AB_2305314
Anti-RIPK3	WEHI	Clone 8G7
Anti-TGN 38	Santa Cruz	Cat#: sc-166594; RRID: AB_2287347
Anti-Ubiquitin	Cell Signaling Technology	Cat#: 3936; RRID: AB_331292
Bacterial and virus strains		
E. coli BL21-Codon Plus (DE3)	This paper	N/A
Salmonella Typhimurium strain SL1344	From the laboratory of Marc Pellegrini	N/A
Chemicals, peptides, and recombinant proteins		
3x FLAG Peptide	APExBio	A6001
Bafilomycin A1	Enzo Life Sciences	BML-CM110-0100
Biotinylated Wheat Germ Agglutinin (WGA)	Sigma-Aldrich	L5142
DyLight650-conjugated streptavidin	ThermoFisher	84547
Glutathione Sepharose 4B	GE Healthcare	GEHE17-0756-01
GSK'872	SynKinase	SYN-5481
GST-TUBE recombinant protein	This paper; generated in-house	N/A
GST-UBA recombinant protein	Gift from the laboratory of J. Silke	N/A

Continued

REAGENT or RESOURCE	SOURCE	IDENTIFIER
Hoechst 33342	ThermoFisher	H3570
Human Fc-TNF	Gift from the laboratory of J. Silke	N/A
IDN-6556 (Emricasan)	Tetralogic Pharmaceuticals	N/A
Immobilon Western Chemiluminescent HRP Substrate	Merck	WBKLS0500
Lipofectamine 2000	ThermoFisher	11668-019
MG-132	Sigma-Aldrich	M7449
MitoTracker™ Deep Red FM	Invitrogen	M22426
Necrostatin-1S	Merck	504297
Q-VD-OPH	MP Biomedicals	SKU 03OPH10901
SlowFade Gold Antifade reagent	ThermoFisher	S36937
SMAC-mimetic Compound A	TetraLogic Pharmaceuticals	N/A
USP21 recombinant protein	Gift from the laboratory of J. Silke	N/A
Experimental models: Cell lines		
Human: 293T	ATCC	CRL-3216
Mouse: MDF	This paper	N/A
Mouse: YAMC	Gift from the laboratory of R. Ramsay.	N/A
Experimental models: Organisms/strains		
Mouse: Wildtype: C57BL/6J	In-house	JAX stock #000664
Mouse: *Ripk3*$^{K469R/K469R}$	In-house, this paper	N/A
Oligonucleotides		
For the list of oligonucleotides, please refer to "Plasmids, mutagenesis, and transfection" section below	This paper	N/A
Recombinant DNA		
Plasmid: HA-GFP	This paper	N/A
Plasmid: HA-Ubiquitin WT	This paper	N/A
Plasmid: HA-Sumo2 WT	Addgene	#48967
Plasmid: HA-Sumo3 WT	Addgene	#17361
Plasmid: PF TRE3G FLAG-mouse RIPK3-WT	This paper	N/A
Plasmid: PF TRE3G FLAG-mouse RIPK3-K5R	This paper	N/A
Plasmid: PF TRE3G FLAG-mouse RIPK3-K30R	This paper	N/A
Plasmid: PF TRE3G FLAG-mouse RIPK3-K56R	This paper	N/A
Plasmid: PF TRE3G FLAG-mouse RIPK3-K63R	This paper	N/A
Plasmid: PF TRE3G FLAG-mouse RIPK3-K145R	This paper	N/A
Plasmid: PF TRE3G FLAG-mouse RIPK3-K158R	This paper	N/A
Plasmid: PF TRE3G PF TRE3G FLAG-mouse RIPK3-K264R	This paper	N/A
Plasmid: PF TRE3G FLAG-mouse RIPK3-K287R	This paper	N/A
Plasmid: PF TRE3G FLAG-mouse RIPK3-K307R	This paper	N/A
Plasmid: PF TRE3G FLAG-mouse RIPK3-K359R	This paper	N/A
Plasmid: PF TRE3G FLAG-mouse RIPK3-K469R	This paper	N/A
Plasmid: PF TRE3G FLAG-mouse RIPK3-K158R/K359R		
Plasmid: PF TRE3G FLAG-mouse RIPK3-K359R/K469R	This paper	N/A

Continued

REAGENT or RESOURCE	SOURCE	IDENTIFIER
Deposited Data		
Mass spectrometry proteomics data	This paper	PRIDE partner repositry: PXD026533
Software and algorithms		
Software: FIJI	ImageJ	https://imagej.net/Fiji
Software: FlowJo	FlowJo	https://www.flowjo.com/
Software: Image Lab	Biorad	https://www.bio-rad.com
Software: PyMOL	PyMOL	https://www.pymol.org/2/
Software: GraphPad PRISM (Version 8.4.3)	GraphPad	https://www.graphpad.com/

RESOURCE AVAILABILITY

Lead contact

Any request for resources or reagents should be directed to the Lead Contact, James E. Vince (vince@wehi.edu.au).

Materials availability

All unique reagents generated in this study are available from the lead contact with a completed materials transfer agreement.

Data and code availability

This paper does not report original code.

The mass spectrometry proteomics data have been deposited to the ProteomeXchange Consortium via the PRIDE partner repository with the dataset identifier PXD026533.

Any additional information required to reanalyze the data reported in this paper is available from the lead contact upon request.

EXPERIMENTAL MODEL AND SUBJECT DETAILS

Animal housing and ethics

All mice were housed at the Walter and Eliza Hall Institute of Medical Research (WEHI), Australia. Animal rooms were monitored to maintain suitable environmental conditions for the mice. Temperature was maintained at approximately 21°C with a band range$\pm$3°C (from 18–24°C). Light cycle was timed as 14/10 h light/dark cycle. Humidity was monitored within the facility and mirrored levels outside the building. Preferred ranges were between 40–70%. Ranges that fell beyond these measures led to increased monitoring of cage conditions within the facility. Air handling units were monitored and alarmed by Facilities Management to provide 16 air changes per hour. The WEHI Animal Ethics Committee approved all experiments in accordance with the Prevention of Cruelty to Animals Act (1986) and the Australian National Health and Medical Research Council Code of Practice for the Care and Use of Animals for Scientific Purposes (1997).

Mice

The C57BL/6J mouse strain was used in this research project. $Ripk3^{K469R/K469R}$ mice were generated on a C57BL/6J background using CRISPR/Cas9 technology by the Melbourne Advanced Genome Editing Center (MAGEC) at WEHI, following a similar methodology as previously published (Lalaoui et al., 2020; Vijayaraj et al., 2021). Briefly, to generate $Ripk3^{K469R/K469R}$ mice, 20 ng/μL of Cas9 mRNA, 10 ng/μL of sgRNA (GAACTGTGCTTGGTCATACT) and 40 ng/μL of oligo donor (TGCAGATTGGGAACTACAACTCCTTG GTAGCACCACCAAGAACTACTGCCTCAAGTTCGGCCCGTTATGACCAAGCACAGTTCGGCAGGGGTA GGGGCTGGCAGCCCTTCCACAAGTAGACTTCA) were injected into the cytoplasm of fertilized one-cell stage embryos derived from WT C57BL/6J breeders. Viable founder mice were identified by next-generation sequencing. Targeted animals were backcrossed onto wildtype C57BL/6J animals for 2 generations to eliminate potential sgRNA off-target hits, and then subjected to a further round of next-generation

sequencing. Mice were routinely genotyped using genomic DNA extracted from tail biopsies using the Direct PCR Lysis tail reagent (Viagen) supplemented with 5 mg/mL proteinase K (Worthington), in accordance with the manufacturer's instructions. The following primers were used to amplify and distinguish between WT *Ripk3* and *Ripk3*$^{K469R/K469R}$ alleles by PCR method: 5′-CTCAAGTTCGGCCAAG-3′ (*Ripk3*$^{+/+}$ forward), 5′-CTCAAGTTCGGCCCGT-3′ (*Ripk3*$^{K469R/K469R}$ forward), 5′-GACTTTAAGGAGATGGGTCAAG-3′ (*Ripk3* common reverse).

Cell lines and culture conditions

Macrophages and dermal fibroblasts were derived from both male and female mice aged anywhere from 6 to 16 weeks. MDFs immortalized with SV40 large T antigen or *Ripk3*$^{-/-}$ bone marrow derived macrophages (BMDMs) immortalized with Cre-J2 virus (*Ripk3*$^{-/-}$ iBMDMs) were cultured in Dulbecco's modified Eagle's medium (DMEM) supplemented with 8% (v/v) fetal calf serum (FCS), 50 U/mL penicillin and 50 U/mL streptomycin at 37°C and 10% (v/v) CO$_2$. YAMC cells, kindly provided by Robert Ramsay (Peter MacCallum Cancer Center), were grown in RPMI media containing 8% v/v FCS, GlutaMAX (ThermoFisher #35050061), 50 U/mL penicillin and 50 U/mL streptomycin at 37°C and 10% (v/v) CO$_2$. WT, *Ripk3*$^{-/-}$ and *Mlkl*$^{-/-}$ MDFs were generated from C57BL/6 mice as previously described (Hildebrand et al., 2014; Murphy et al., 2013; Newton et al., 2004). All cell lines were routinely monitored for mycoplasma contamination.

Primary BMDMs were generated from the femoral and tibial bone marrow cells of WT and *Ripk3*$^{K469R/K469R}$ C57BL/6 mice. Upon harvest, bone marrow cells were cultured on 15 cm bacterial Petri dishes for 7 days in DMEM supplemented with 20% L929 conditioned media and 8% (v/v) FCS at 37°C and 10% (v/v) CO2. Fresh media was added on day 3, and cells harvested, counted and used in experiments on day 6 or 7.

For generation of primary MDFs, the dermis layer of a whole skin tail was separated from the epidermis layer by incubating with 2.1 U/mL Dispase II (Sigma; D4693) in serum-free DMEM media at 37°C for 2 h. The dermis was then incubated in 0.025 mg/mL Liberase TM (Sigma, 5401119001) in serum-free DMEM media at 37°C for 1.5 h with shaking. The following day, the dermis was passed through a 100 μm Falcon sieve by using a sterile plastic syringe plunger and washed thoroughly with 8% FCS-supplemented DMEM media. Cells were grown and used for experiments for up to 2 weeks before they entered senescence.

METHOD DETAILS

Mouse model of *Salmonella* infection

Mice used in these experiments were a mix of littermate and non-littermate animals of both sexes aged 7–9 weeks, and both groups of WT mice were confirmed to respond similarly to infection. A single colony of *Salmonella* BRD509 was cultured overnight in Luria Bertani (LB) broth containing 50 μg/mL Streptomycin (Sigma-Aldrich) in a shaking incubator at 37°C, then sub-cultured in fresh LB broth (+Streptomycin) for 3 h under the same conditions. Bacteria were pelleted at 4000 xg for 20 min, then resuspended in PBS and measured by absorbance at OD$_{600}$ to extrapolate colony forming units (CFU)/mL (i.e. 1 × 10^9 CFU/mL= OD$_{600}$ 1.0). WT control and *Ripk3*$^{K469R/K469R}$ mice were infected with *S. Typhimurium* BRD509 at 100 CFU by intravenous (iv) injection. Mice were culled and organs harvested 14 days post-infection. Serum was extracted from cardiac bleeds for multiplex cytokine analysis using the BD Cytometric Bead Array Mouse Inflammation Kit (BD Bioscience). Organs from infected mice were weighed and homogenised in 2 mL (spleens) or 5 mL (livers) of PBS. Homogenates were serially diluted (in duplicate) in PBS and 10 μL drops plated out in duplicate onto LB agar (+Streptomycin) and incubated overnight at 37°C. CFU/mL was calculated per organ for each mouse and then standardised to CFU/mg organ based on organ weights. Injections and analyses were performed in a blinded manner to mouse genotypes.

Salmonella infection of BMDMs

Studies were performed as previously described using *Salmonella* Typhimurium strain SL1344 (Doerflinger et al., 2020). Bacteria were grown at 37°C for 16–18h under 50 μg/mL Streptomycin antibiotic selection. Multiplicity of infection (MOI) was calculated based on the OD600 reading, whereby OD600 = 1 = 10^9 CFU of bacteria/mL. An MOI 10 with 50,000 cells, for example, equates to 0.5 μL of the bacterial culture in the cell media. Cells were infected in antibiotic-free DMEM for 30 min. Then, cell supernatants were harvested for a 30 min time-point, or washed twice with PBS and replaced in DMEM supplemented

with 20% L929 conditioned media, 8% (v/v) FCS, and 50 μg/mL Gentamycin. Cells were incubated for a further 60 min for a 2 h time-pointprior to cell supernatant harvest. LDH analysis was performed with the CytoTox 96® Non-Radioactive Cytotoxicity Assay (Promega, G1780) according to the manufacturer's instructions.

Compounds and antibodies

The following compounds were utilized in this study: Bafilomycin A1 (Baf-A$_1$, Enzo Life Sciences #BML-CM110-0100), recombinant human TNF-Fc [made in-house (Bossen et al., 2006)], SMAC-mimetic Compound A (Cp.A; TetraLogic Pharmaceuticals), Necrostatin-1S (Nec-1$_S$; Merck #504297), pan-caspase inhibitors Q-VD-OPH (MP Biomedicals #SKU 03OPH10901) and IDN-6556 (provided by Tetralogic Pharmaceuticals), doxycycline (dox; Sigma-Aldrich), GSK'872 (SynKinase #SYN-5481), and MG-132 (Sigma-Aldrich; M7449).

Primary antibodies used in this study were: mouse anti-β-actin (Sigma-Aldrich #A1987; 1:5000), rabbit anti-Calreticulin (CST #12238), rabbit-*anti*-caspase-3 (CST #9662), rabbit-*anti*-cleaved caspase-3 (D175) (CST #9579), rabbit-*anti*-cleaved caspase-8 (D387) (CST #8592), mouse-*anti*-flotilin-1 (BD Transduction Laboratories #610821), rabbit anti-GAPDH (Merck #MAB374; 1:5000), mouse anti-GM130 (BD Transduction Laboratories #610822; 1:200 for microscopy), rat anti-HA (Roche #11867423001), rabbit-*anti*-Lamin A/C (Santa Cruz #sc-20681), rat anti-LAMP 1 (Santa Cruz #sc-19992; 1:300 for microscopy), rat anti-MLKL (WEHI clone 3H1 (Murphy et al., 2013) and available from Merck #MABC604; 1 μg/mL), rabbit-*anti*-p-MLKL^{S345} (Abcam #196436/CST #37333), rabbit anti-p-RIPK3$^{T231/S232}$ (Genentech #GEN-135-35-9 (Newton et al., 2016b); 1 μg/mL for western blotting or 5 μg/mL for microscopy), rabbit anti-RIPK1 (CST #3493), rat anti-RIPK3 (WEHI clone 8G7 (Petrie et al., 2019); 1:2000 for western blotting or 1:1000 for microscopy), mouse anti-TGN 38 (Santa Cruz #sc-166594; 1:300 for microscopy), rabbit anti-Ubiquitin (CST #3936). All primary antibodies were used at a 1:1000 dilution unless stated otherwise.

Secondary antibodies used in this study were: HRP-conjugated anti-rabbit IgG (Southern Biotech #4010-05; 1:10000), HRP-conjugated anti-rat IgG (Southern Biotech #3010-05; 1:10000), HRP-conjugated anti-mouse IgG (Southern Biotech #1010-05; 1:10000), AlexaFluor 488-conjugated anti-rabbit IgG (Invitrogen #A-11008; 1:1000), AlexaFluor 594-conjugated anti-rat IgG (Invitrogen #A-11007; 1:1000), AlexaFluor 594-conjugated anti-mouse IgG (Invitrogen #R37121; 2 drops/mL) and AlexaFluor 647-conjugated anti-rabbit IgG (Invitrogen #A-31573; 1:1000).

Plasmids, mutagenesis, and transfection

HA-GFP was cloned into pcDNA5.5, while HA-Ubiquitin WT was cloned into pEF6/Myc-His. Both vectors were kind gifts from Pascal Meier. HA-Sumo2 (Addgene #48967) and HA-Sumo3(Addgene #17361) constructs were kindly provided by Guy Salvesen (Bekes et al., 2011) and Edward Yeh (Kamitani et al., 1998), respectively. All constructs were transiently transfected into 293T cells following the Lipofectamine 2000 Transfection protocol (ThermoFisher 11668-019).

RIPK3-WT, -K5R, -K30R, -K56R, -K63R, -K145R, -K158R, -K264R, -K287R, -K307R were synthesized by ATUM (California, US), while RIPK3-K359R, -K469R, -K158R/K359R, and -K359R/K469R were generated by the PCR-directed overlap extension technique (Heckman and Pease, 2007). For RIPK3-K158R/K359R, K359R was introduced using RIPK3-K158R as the DNA template. Two primer pairs (denoted pair AB and pair CD) were designed with a 36–42°C melting temperature on each side of the desired base pair change, assuming each A or T base pair is 2°C, and G or C base pair is 4°C. To obtain the final DNA product containing the desired mutation, products from AB and CD primer pairs were combined together in equal amounts, and the reaction was repeated to create AD product using primers A (Sense sequence) and D (Anti-sense sequence).

All constructs were cloned into an N-terminal FLAG-tagged doxycycline-inducible pF TRE3G PGK puro plasmid, as previously described (Moujalled et al., 2013, 2014; Murphy et al., 2013). Lentivirus was generated using Effectene Transfection Reagent (QIAGEN) in HEK293T cells, and target cells were infected in media containing 4 μg/mL Polybrene. Cells were selected in 5 μg/mL puromycin.

Primer Sequences Used in PCR.

RIPK3 Target	Sense (5′-3′)	Anti-sense (5′-3′)
K359R (pair AB)	CGCGGATCCTCTGTCAAGTTATGGCCTAC	CCTCTCAGGACATCTTCCAGGAACTGG
K359R (pair CD)	CCAGTTCCTGGAAGATGTCCTGAGAGG	GCGGAATTCACTTGTGGAAGGGCTGC
K469R (pair AB)	GGATCTGCGCCACCATGGATTAC	GTGCTTGGTCATACCTGGCCGAACTTG
K469R (pair CD)	CAAGTTCGGCCAGGTATGACCAAGCAC	CTAGTGAGACGTGCTACTTCCATTTGTC

Recombinant protein purification of GST-UBA and GST-TUBE

The recombinant GST-tagged Ubiquillin-UBA1x (UBA) and Ubiquillin-UBA4x (TUBE) were expressed from pGEX-6P1 plasmids encoding the respective protein, and have been described elsewhere (Hjerpe et al., 2009). The pGEX-6P1 plasmid encoding GST-TUBE was kindly provided by David Komander. Briefly, proteins were expressed with 0.3 mM IPTG in *E. coli* BL21-Codon Plus (DE3) at 18°C overnight. Cells were lysed by sonication in Buffer A [50 mM Tris pH 8.0, 50 mM NaCl, 1 mM EDTA, 1 mM DTT, 10% glycerol, and complete protease inhibitor cocktail (Roche)]. Lysates were clarified by centrifugation at 45000 xg for 30 min prior to standard glutathione agarose affinity purification protocol (GE Healthcare). Elution was performed twice with 10 mM reduced glutathione in Buffer A at 4°C with rotation for 30 min.

Flow cytometry

Upon harvest, cells were stained with 0.5 μg/mL propidium iodide (PI) and subsequently analyzed with a BD FACS Calibur instrument (BD Biosciences). Data were analyzed using FlowJo software.

IncuCyte live-cell imaging

To assess cell viability using the IncuCyte S3 (Sartorius) system, cells were seeded in triplicate in 96-well plates and were incubated in SYTOX™ Green Nucleic Acid Stain (ThermoFisher #S7020) at 0.5 μM and SPY650-DNA (Spirochrome) at a 2000x dilution. The algorithm setting was adjusted to accurately detect green and red puncta. To calculate the % Sytox positive cells (i.e. cell death), the puncta count for the green channel was divided by the red channel count and the result multiplied by 100.

Clonogenic survival assays

Assays was conducted as previously described (Franken et al., 2006). Briefly, cells were seeded on a 6-well plate at 1,500 cells/well, and stimulated with 10 ng/mL dox as indicated over 7 days. On harvest, cells were fixed with 100% methanol for 5 min, methanol removed, and cells subsequently stained with 0.1% w/v crystal violet for 30 min.

Confocal imaging

Cells were seeded in 8-well μ-slides (Ibidi #80826) and treated as indicated. For plasma membrane staining, 2 μL of biotinylated wheat germ agglutinin (WGA; Sigma-Aldrich #L5142) was added to each well 10 min prior to harvest. For mitochondria staining, cells were incubated with 100 nM MitoTracker Deep Red FM (Invitrogen M22426) for 30 min prior to fixation. On harvest, cells were fixed with 4% PFA in PBS for 10 min, washed with PBS, and permeabilized with 0.1% saponin, 10% donkey serum in TBS (0.2 μm filtered) for 30 min. Fixed samples were then incubated in primary antibodies as indicated for overnight at 4°C. The next day, samples were washed twice in PBS, incubated in secondary antibodies for 1h at room temperature and 20 min prior to washing, 2 μg/mL of Hoechst 33348 (ThermoFisher #H3570) was applied. For WGA detection, 1–2 μg/mL DyLight650-conjugated streptavidin (ThermoFisher #84547) was used during the secondary antibody incubation step. After 2 washes with PBS, samples were mounted with SlowFade Gold Antifade reagent (ThermoFisher #S36937). All images were obtained using a 63x oil objective on a confocal laser scanning Leica TCS SP8 microscope with z-stacks, and subsequently analyzed using FIJI software.

FLAG and HA immunoprecipitation (IP)

For FLAG IP analysis, MDFs were seeded in 2 × 15 cm plates at 80% confluency. After dox stimulation, cells were harvested and lysed in DISC buffer (1% Triton X-100, 150 mM NaCl, 20 mM Tris pH 7.5, 10% glycerol, 2 mM EDTA) supplemented with complete protease inhibitor cocktail (Roche) for 20 min on ice. Samples were clarified by centrifugation (21000 xg for 5 min), and the soluble cell lysate incubated with 20 μL of packed magnetic anti-FLAG beads (Sigma) per 15 cm plate at 4°C with rotation overnight. Upon 2 washes

with DISC buffer, samples were eluted twice in 1 mg/mL 3x FLAG peptide (APExBio) in TBS pH 7.5. The combined eluate was mixed with SDS lysis buffer for further analysis by western blotting.

For HA IP analysis, 293Ts were seeded in 6-well plates at 80% confluency. Cells were transiently co-transfected with the appropriate HA construct and FLAG RIPK3-WT. Cells were stimulated with 20 ng/mL dox overnight post-transfection, harvested and lysed in DISC buffer. Samples were processed similar to the FLAG IP, except that they were incubated in 20 μL of packed magnetic anti-HA beads (ThermoFisher), and the beads were lysed directly in SDS lysis buffer after completing the incubation and two wash steps.

Liquid chromatography–tandem mass spectrometry (LC-MS/MS)

MDFs were seeded in 4 × 15 cm plates at 80% confluency, stimulated with 20 ng/mL dox overnight, lysed in DISC buffer, and FLAG-purified as described above, except that samples were washed twice in MS buffer (1% Triton X-100, 1 M urea, 500 mM NaCl, 20 mM Tris pH 7.5, 10% glycerol, 2 mM EDTA) at 4°C with rotation for 15 min. Eluted samples were subjected to tryptic digestion, following the FASP protocol described previously (Wisniewski et al., 2009).

Samples were analyzed on an M-class UPLC (Waters, USA) coupled to a timsTOF Pro (Bruker, Germany) equipped with a CaptiveSpray source. Peptides were resuspended in 2% ACN, 1% formic acid (FA) separated on a 25 cm × 75 μm analytical column, 1.6μm C18 beads with a packed emitter tip (Aurora Series, IonOpticks, Australia). The column temperature was maintained at 50°C using an integrated column oven (Sonation GmbH, Germany). The column was equilibrated using 5 column volumes before loading sample in 100% buffer A (99.9% MilliQ water, 0.1% FA). Samples were separated at 400 nL/min using a linear gradient from 2% to 17% buffer B (99.9% ACN, 0.1% FA; 55min), 17%–25% buffer B (21min) before ramping to 35% buffer B (13min), ramp to 85% buffer B (3min) and sustained for 10min. The timsTOF Pro (Bruker) was operated in PASEF mode using Compass Hystar 5.0.36.0. Alternatively, samples were resuspended in 2% acetonitrile, 1% formic acid and injected and separated by reversed-phase liquid chromatography on an M-class UPLC system (Waters, USA) using a 250 mm × 75 μm column (1.6μm C18, packed emitter tip; IonOpticks, Australia) with a linear 90-min gradient at a flow rate of 400 nL/min from 98% solvent A (0.1% Formic acid in Milli-Q water) to 34% solvent B (0.1% Formic acid, 99.9% acetonitrile). The UPLC was coupled on-line to a Q-Exactive mass spectrometer (Thermo Fisher, USA). The Q-Exactive was operated in a data-dependent mode, switching automatically between one full-scan and subsequent MS/MS scans of the 10 most abundant peaks. Full-scans (m/z 350–1,850) were acquired with a resolution of 70,000 at 200 m/z. The 10 most intense ions were sequentially isolated with a target value of 100,000 ions and an isolation width of 2 m/z and fragmented using HCD with normalized collision energy of 27. Maximum ion accumulation times were set to 50ms for full MS scan and 50ms for MS/MS. Dynamic exclusion was enabled and set to 20 s.

Raw files were analyzed using MaxQuant (version 1.6.10.43). The database search was performed using the Uniprot *Mus Musculus* database plus common contaminants with strict trypsin specificity allowing up to 2 missed cleavages. The minimum peptide length was 7 amino acids. Carbamidomethylation of cysteine was a fixed modification while N-acetylation of proteins N-termini, oxidation of methionine and diGly motif of Lysine were set as variable modifications. During the MaxQuant main search, precursor ion mass error tolerance was set to 6 ppm. PSM and protein identifications were filtered using a target-decoy approach at a false discovery rate (FDR) of 1% with the match between runs option enabled.

Further analysis was performed using a custom pipeline developed in R, which utilizes the MaxQuant output files. A feature was defined as the combination of peptide sequence, charge and modification. Features not found in at least 50% of the replicates in one group were removed. To correct for injection volume variability, feature intensities were normalized by converting to base 2 logarithms and then multiplying each value by the ratio of maximum median intensity of all replicates over median replicate intensity. Missing values were imputed using a random normal distribution of values with the mean set at mean of the real distribution of values minus 1.8 s.d., and a s.d. of 0.3 times the s.d. of the distribution of the measured intensities. The probability of differential peptide expression between groups was calculated using the Limma R package. Probability values were corrected for multiple testing using Benjamini–Hochberg method. The mass spectrometry proteomics data have been deposited to the ProteomeXchange Consortium via the PRIDE partner repository with the dataset identifier PXD026533.

Purification of the ubiquitylated proteome

To purify ubiquitylated substrates, 50 μg/mL of GST-UBAs or GST-TUBEs per experimental condition was pre-bound to glutathione Sepharose beads (GE Healthcare) for 30 minutes at 4°C with rotation. Approximately 2 × 10^6 cells per condition were lysed in urea lysis buffer (4 M urea, 50 mM Tris pH 7.5, 120 mM NaCl, 1% NP-40, 1 mM EDTA) for 10 min on ice for efficient extraction of RIPK3. Samples were centrifuged (21000 xg for 5 min) to remove the remaining insoluble protein/lipid aggregates, and the soluble cell lysate was diluted in Wash Buffer (50 mM Tris pH 7.5, 120 mM NaCl, 1% NP-40, 1 mM EDTA) at a ratio of 1:1 to dilute the urea to 2M. Lysates were then incubated with 10–20 μL of packed GST-UBA or GST-TUBE beads at 4°C overnight while rotating. Beads were then washed twice in Wash Buffer, followed by resuspension in 2x reducing SDS lysis buffer. Samples were heated at 56°C or 65°C for 15 min, followed by a 17000 xg centrifugation for 5 min, prior to SDS-PAGE and western blot analysis. In the case of GST-TUBE pulldown of TX-100-fractionated cells, cells were lysed in DISC buffer for 20 min on ice. Upon centrifugation at 17000 xg for 5 min, soluble cell lysate was incubated with 10–20 μL of packed GST-TUBE beads, while the pellet was further lysed in 4M urea, and processed as above. All buffers were supplemented with 10 mM N-ethylmaleimide and complete protease Inhibitor Cocktail (Roche).

USP21 assay

USP21 DUB was activated in DUB reaction buffer (50 mM Tris pH 7.5, 50mM NaCl and 5 mM DTT) for 10 minutes at room temperature. Approximately 2 × 10^6 cells per condition were lysed and GST-UBA (50 μg/mL per condition) used to purify the ubiquitylated proteins as described above. After incubation and washing (as outlined above), beads were incubated in 3 μM of activated USP21 at 37°C for 1 h. The reaction was stopped by addition of 2x reducing SDS lysis buffer and samples analyzed by western blot.

Western blotting

For whole cell lysates, cells were lysed directly in reducing SDS lysis buffer. All samples were resolved by SDS-PAGE on either 4–12% NuPAGE Novex Bis-Tris (Invitrogen) or 4–15% Criterion TGX Stain-Free gels (Biorad), and protein transferred onto nitrocellulose or PVDF membranes. Membranes were blocked in 5% w/v skim milk in PBS containing 0.1% Tween-20 (PBST) for 10 min, and probed with the relevant primary antibodies overnight. Membranes were then incubated in secondary antibodies for 1 h, and developed using ECL (Milipore), and detected with an X-OMAT film developer, or the ChemiDoc Touch Imaging System (BioRad) coupled with Image Lab Software (Biorad). All primary antibodies were diluted in 5% w/v BSA-containing PBST, while the secondary antibodies were diluted in 5% w/v skim milk in PBST. All membranes were washed 3 times with PBST after antibody incubations.

QUANTIFICATION AND STATISTICAL ANALYSIS

Each data point from graphs represents an independent experiment, acquired either on different days or performed by different scientists, or an independent biological replicate (i.e. a different mouse), as indicated in the figure legends. *In vitro* experiments are displayed as the mean ± SE of the mean (SEM). The *in vivo* data was collected with the researchers blinded to genotype and are pooled from two independent experiments and depicted as the mean ± SEM Statistical analysis on the *in vivo* data was performed with a Mann-Whitney test using GraphPad PRISM (Version 8.4.3). A statistical analysis of the *in vitro* data was not performed due to the small sample size and the arbitrary *p* value threshold assigned to significance being potentially misleading (Amrhein et al., 2019).